

# Visualization of the mechanosensitive ion channel MscS under membrane tension

<https://doi.org/10.1038/s41586-021-03196-w>

Received: 25 February 2020

Accepted: 6 January 2021

Published online: 10 February 2021

 Check for updates

Yixiao Zhang<sup>1</sup>, Csaba Daday<sup>2</sup>, Ruo-Xu Gu<sup>2</sup>, Charles D. Cox<sup>3,4</sup>, Boris Martinac<sup>3,4</sup>, Bert L. de Groot<sup>2</sup> & Thomas Walz<sup>1</sup>✉

Mechanosensitive channels sense mechanical forces in cell membranes and underlie many biological sensing processes<sup>1–3</sup>. However, how exactly they sense mechanical force remains under investigation<sup>4</sup>. The bacterial mechanosensitive channel of small conductance, MscS, is one of the most extensively studied mechanosensitive channels<sup>4–8</sup>, but how it is regulated by membrane tension remains unclear, even though the structures are known for its open and closed states<sup>9–11</sup>. Here we used cryo-electron microscopy to determine the structure of MscS in different membrane environments, including one that mimics a membrane under tension. We present the structures of MscS in the subconducting and desensitized states, and demonstrate that the conformation of MscS in a lipid bilayer in the open state is dynamic. Several associated lipids have distinct roles in MscS mechanosensation. Pore lipids are necessary to prevent ion conduction in the closed state. Gatekeeper lipids stabilize the closed conformation and dissociate with membrane tension, allowing the channel to open. Pocket lipids in a solvent-exposed pocket between subunits are pulled out under sustained tension, allowing the channel to transition to the subconducting state and then to the desensitized state. Our results provide a mechanistic underpinning and expand on the ‘force-from-lipids’ model for MscS mechanosensation<sup>4,11</sup>.

Bacterial mechanosensitive channels protect bacteria from osmotic lysis by opening upon a sudden drop in environmental osmolarity<sup>12–14</sup>. MscS is one of the most extensively studied mechanosensitive channels<sup>5–8</sup>. Membrane tension opens the channel, either fully or to a subconducting state<sup>15,16</sup>, and if tension persists, MscS transitions into a non-conductive desensitized state<sup>6,15,17–19</sup>. The structure of MscS is known in the closed and open states<sup>9,10,20–23</sup> (Extended Data Fig. 1a, b). It forms a homo-heptamer with a large cytoplasmic domain and each subunit contributes three transmembrane helices (TMs): TM3a, separated from TM3b by a kink, lines the pore; and TM1 and TM2 form a helical hairpin (TM1–TM2) that faces the lipid bilayer. The closed-to-open transition is accompanied by an approximately 18° increase in the tilt angle of TM1–TM2 relative to the membrane normal and a 50° rotation about the symmetry axis, increasing the pore diameter from 5 to 14 Å (refs. <sup>9,10</sup>). In addition, the size of the hydrophobic pockets formed by neighbouring TM1–TM2 domains and a TM3b decreases in the open conformation<sup>9,10</sup>.

Recent studies have focused attention on the role of lipids in mechanosensation. In the TRAAK channel, membrane tension appears to remove a lipid acyl chain that blocks the pore in the closed state<sup>24</sup>, and changes in membrane curvature have a role in opening the PIEZO1 channel<sup>25</sup>. For MscS, molecular dynamics simulations have shown that its hydrophobic pockets are filled by different numbers of lipids in the open and closed states, prompting the ‘lipids-move-first’ model<sup>22</sup> in which membrane tension pulls lipids out of the hydrophobic pockets,

causing TM1–TM2 to tilt and the channel to open—thus providing a molecular model for how the force-from-lipid principle may apply to MscS. Two recent structures of MscS in nanodiscs confirmed the structure of MscS in the closed conformation and resolved bound lipids<sup>11,26</sup>, but the role of the lipids and the mechanism underlying tension-induced channel opening remained unclear. Here we determined the structures of MscS in different membrane environments, including one that mimicked membrane tension, allowing us to complete the conformational cycle of MscS (Supplementary Videos 1, 2) and to propose roles for the bound lipids in mechanosensation. Our structural data are supported by functional data obtained from patch-clamp recordings of MscS reconstituted into azolectin liposomes.

## MscS in PC-18:1 lipids is closed

We first reconstituted MscS into nanodiscs with dioleoyl phosphatidylcholine (PC-18:1), a lipid that has previously been used for functional studies of MscS<sup>22,27,28</sup>, and determined the cryo-electron microscopy (cryo-EM) structure of MscS–PC-18:1 at 3.2 Å resolution (Extended Data Figs. 1c–e, 2a, 5). MscS in a PC-18:1 bilayer adopts the closed conformation seen in crystal structures, but we observed additional density at the N terminus that we assigned to residues 15–27 and modelled as an amphipathic helix (Extended Data Fig. 2b–f, Supplementary Information). As amphipathic helices are also present in other mechanosensitive channels<sup>24,29,30</sup>, membrane-associated helices may contribute to

<sup>1</sup>Laboratory of Molecular Electron Microscopy, The Rockefeller University, New York, NY, USA. <sup>2</sup>Department of Theoretical and Computational Biophysics, Max Planck Institute for Biophysical Chemistry, Göttingen, Germany. <sup>3</sup>St Vincent’s Clinical School, University of New South Wales, Sydney, New South Wales, Australia. <sup>4</sup>Molecular Cardiology and Biophysics Division, Victor Chang Cardiac Research Institute, Sydney, New South Wales, Australia. ✉e-mail: [twalz@rockefeller.edu](mailto:twalz@rockefeller.edu)

linking changes in membrane tension to conformational changes in these channels.

### MscS in PC-10 lipids is partially open

Tension will cause membranes to become thinner<sup>1,31</sup>, creating a hydrophobic mismatch with the embedded membrane proteins. To test whether MscS would adapt to a thinner lipid bilayer by increasing the tilt of TM1–TM2, which could open the channel, we reconstituted MscS into nanodiscs with didecanoyl phosphatidylcholine (PC-10) and determined the structure of MscS–PC-10 at 3.4 Å resolution (Fig. 1a, Extended Data Figs. 3, 5). Measured as the angle between TM1 and the membrane normal, the tilt of TM1–TM2 in the very thin PC-10 bilayer was 56°, which was higher than in the closed (32°) and even in the open conformation (50°) (Fig. 1a). Even though residues 1–24 are not resolved in MscS–PC-10, the high tilt of TM1–TM2 clearly results in a contracted transmembrane domain (TMD).

TM1–TM2 was not only more tilted but was also rotated relative to the constant cytoplasmic domain (Fig. 1a, b). In the closed state, TM1–TM2 was aligned with TM3b of the neighbouring subunit (that is, domain-swapped) but in MscS–PC-10, TM1–TM2 was aligned with TM3b of the same subunit, which was also the case for MscS in the open conformation (Fig. 1a, b). The change in the TM1–TM2 arrangement also affected the pore-forming helix TM3a. In MscS–PC-10, residue Ser95 at the N-terminal end of TM3a swung out by approximately 4 Å into a position in between those in the open and closed conformations (Fig. 1c). As a result, the narrowest pore diameter, at the height of residues Leu105 and Leu109, was 10 Å, which was smaller than in the open conformation (14 Å) but was still wider than in the closed conformation (5 Å) and wide enough to allow ion conduction. On the basis of the greater similarity of the TM1–TM2 arrangement with that in the open conformation and the pore size being in between those of the open and closed states, MscS–PC-10 appeared to show the structure of a partially open channel, presumably representing MscS in a subconducting state. This notion is supported by the fact that MscS reconstituted into azolectin liposomes doped with 30% PC-10 exhibited spontaneous gating events that do not reach the unitary conductance of the fully open channel ( $1.21 \pm 0.04$  nS;  $n = 6$ ) (Fig. 1d, e, Supplementary Information).

### Hydrophobic mismatch does not open MscS

The MscS–PC-10 structure demonstrates that hydrophobic mismatch generated by a very thin membrane can induce channel opening, at least to some degree. However, the hydrophobic thickness of a bilayer formed by PC-10 is only about 15.8 Å (ref. <sup>32</sup>) and a biological membrane will rupture before thinning to this degree. To determine at which membrane thickness the channel would open, we reconstituted MscS into nanodiscs with lipids of different acyl-chain lengths.

Density maps obtained with dimyristoyl phosphatidylcholine (PC-14) (Fig. 1f) and dilauroyl phosphatidylcholine (PC-12) (Fig. 1g) showed that, in these bilayers with calculated hydrophobic thicknesses of 22.8 Å and 19.3 Å, respectively, MscS adopted a closed conformation. Upon reconstitution into nanodiscs with diundecanoyl phosphatidylcholine (PC-11), which has a calculated hydrophobic thickness of 17.5 Å, the predominant class showed MscS in the closed conformation (Fig. 1h). In a minor class, TM1 was slightly more tilted (40°) but also less of the TM1 helix was resolved, and the remainder of the TMD was still in the closed conformation (Fig. 1h). Thus, unless the membrane becomes unphysiologically thin, hydrophobic mismatch alone does not open MscS.

### MscS in the desensitized conformation

As a more direct way to visualize how membrane tension affects MscS, we used β-cyclodextrin (βCD) to remove lipids from the nanodiscs. We reasoned that the remaining bilayer would then have to ‘stretch’ to cover

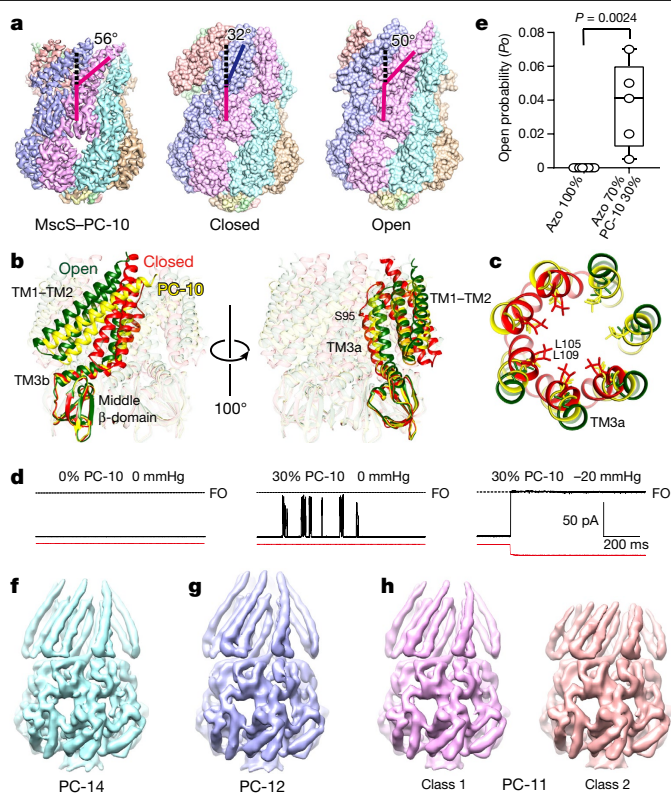


**Fig. 1 | Conformation of MscS in a PC-10 bilayer (MscS–PC-10).** **a**, Cryo-EM maps of MscS in a PC-10 nanodisc (left) and surface representations of the crystal structures of MscS in the closed (middle; Protein Data Bank (PDB): 2OAU) and open (right; PDB: 2VV5) conformations. The lines illustrate the tilt of TM1–TM2 and whether TM3b of one subunit (lower pink line) aligns with the TM1–TM2 of its own subunit (upper pink line) or the neighbouring subunit (upper purple line). **b**, **c**, Comparison of the transmembrane helical arrangement (**b**) and the pore (**c**) in MscS–PC-10 (yellow) with those of MscS in the closed (red) and open (green) conformations. In **b**, the structures are aligned on the basis of the cytoplasmic domain. One subunit is shown in colour. In **c**, MscS–PC-10 is overlaid with both crystal structures in the bottom three subunits and only with the crystal structure of the closed state in the top left two subunits and the crystal structure of the open state in the top right two subunits. The side chains of the gating residues Leu105 and Leu109 are shown as sticks. **d**, Representative traces of MscS reconstituted into azolectin (Azo) liposomes (left), azolectin liposomes doped with 30% PC-10 with no applied hydrostatic pressure (middle) and azolectin liposomes doped with 30% PC-10 with applied pressure (black traces: current, red traces: pressure). FO, fully open. **e**, Open probability of MscS in azolectin liposomes ( $n = 7$ ) and azolectin liposomes doped with 30% PC-10 ( $n = 5$ ) without applied pressure (0 mmHg). The box and whiskers plot shows the minimum to maximum values with the median as the midline. The  $P$  value was determined using unpaired  $t$ -test. **f–h**, Cryo-EM maps of MscS in bilayers formed by PC-14 (**f**), PC-12 (**g**) and PC-11 (**h**). For comparison, all four maps were low-pass-filtered to 6 Å resolution. Although class 2 of MscS in a PC-11 bilayer shows a shorter TM1, the remainder of the density map represents the same closed conformation as all the other density maps.

the surface area encompassed by the membrane scaffold proteins, thus exerting tension on the embedded MscS (Fig. 2a). After establishing that βCD can extract PC-18:1 from nanodiscs (Extended Data Fig. 4a), we incubated MscS-containing PC-18:1 nanodiscs with βCD and used gel filtration to isolate intact MscS-containing nanodiscs for cryo-EM analysis (Extended Data Fig. 4b).

The 2D averages showed that the TMD of MscS in βCD-treated PC-18:1 nanodiscs was much thinner than that of MscS in untreated PC-18:1 nanodiscs (Fig. 2b); thus, we determined a structure at an overall resolution of 3.7 Å (the local resolution of the TM1–TM2 is approximately

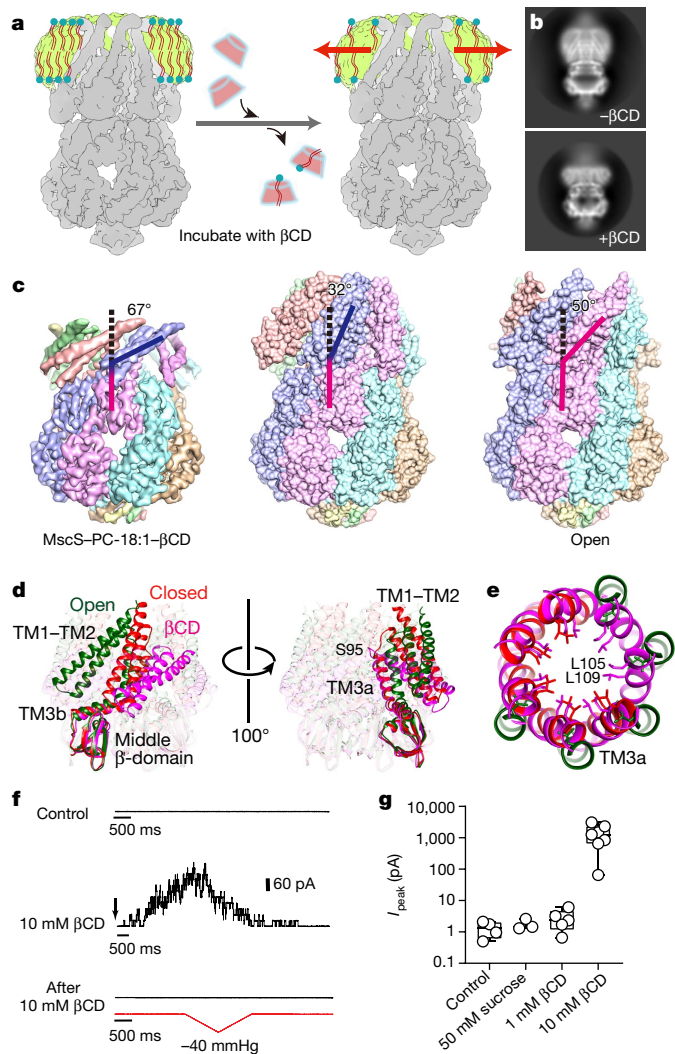


**Fig. 2 | Conformation of MscS in a PC-18:1 bilayer after treatment with  $\beta$ CD (MscS-PC-18:1- $\beta$ CD).** **a**, The principle of creating membrane tension by extracting lipids from a nanodisc with  $\beta$ CD. **b**, The 2D class averages of MscS in a PC-18:1 nanodisc before ( $-\beta$ CD) and after incubation with  $\beta$ CD ( $+\beta$ CD). Side length of individual averages, 20.8 nm. **c**, Cryo-EM maps of MscS in a  $\beta$ CD-treated PC-18:1 nanodisc (left) and surface representations of the crystal structure of MscS in the closed (middle; PDB: 2OAU) and open (right; PDB: 2V55) conformations. The lines illustrate the tilt of TM1-TM2 and whether TM3b of one subunit (lower pink line) aligns with the TM1-TM2 of its own subunit (upper pink line) or the neighbouring subunit (upper purple line). **d, e**, Comparison of the transmembrane helical arrangement (**d**) and the pore (**e**) in MscS-PC-18:1- $\beta$ CD (purple) with those of MscS in the closed (red) and open (green) conformations. In **d**, the structures are aligned on the basis of the cytoplasmic domain. One subunit is shown in colour. In **e**, MscS-PC-18:1- $\beta$ CD is overlaid with both crystal structures in the bottom three subunits and only with the crystal structure of the closed state in the top left two subunits and the crystal structure of the open state in the top right two subunits. The side chains of the gating residues Leu105 and Leu109 are shown as sticks. **f**, Representative recordings (+30 mV) of MscS reconstituted into liposomes showing a comparison between a control with no pressure applied (top), during perfusion of 10 mM  $\beta$ CD (middle) and after the addition of  $\beta$ CD when a pressure ramp of up to -40 mmHg was applied (bottom; black trace: current, red trace: pressure). **g**, The peak currents of MscS measured in the absence of applied pressure (control;  $n = 4$ ), after perfusion of 50 mM sucrose (as a control for a change in osmolarity;  $n = 3$ ) and after perfusion of 1 mM ( $n = 5$ ) and 10 mM ( $n = 7$ )  $\beta$ CD. The box and whiskers plot shows the minimum to maximum values with the median shown as the midline.

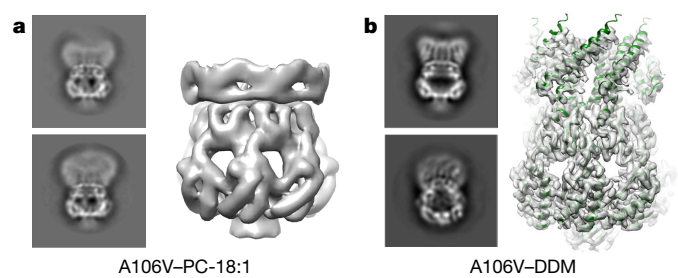


**Fig. 3 | Conformations of MscS with the open-state-stabilizing Ala106Val mutation in nanodiscs and detergent.** **a**, The 2D averages (left) and a typical 3D class (right) of the Ala106Val mutant reconstituted into nanodiscs with PC-18:1. The TMD is smeared out, suggesting that it does not adopt a single defined conformation. See Extended Data Fig. 7c, d for more 2D and 3D classes. Side length of individual averages, 20.8 nm. **b**, The 2D averages (left) and a refined 3D class (right) of the Ala106Val mutant in the detergent dodecyl maltoside (DDM). The refined map (transparent surface) is very similar to the docked crystal structure of the Ala106Val mutant that shows the channel in the open conformation (PDB: 2V55; dark green). See Extended Data Fig. 7e, f for more 2D and 3D classes. Side length of individual averages, 19.7 nm.

5 Å (Fig. 2c, Extended Data Figs. 4c–e, 5). In MscS-PC-18:1- $\beta$ CD, the tilt angle of TM1 was 67°, which was even higher than in MscS-PC-10 (56°). However, unlike in MscS-PC-10, in which TM1-TM2 was aligned with TM3b of the same subunit, as in the open conformation, in MscS-PC-18:1- $\beta$ CD, TM1-TM2 was domain-swapped, as in the closed conformation (Fig. 2c, d). The pore helix TM3a adopted a position similar to the one in the closed conformation, resulting in a pore diameter of 6 Å, which was only slightly wider than in the closed conformation (5 Å) (Fig. 2e). Pore opening is thus not defined by the tilt of TM1-TM2, but depends on whether it interacts with the TM3b of the same subunit or that of the neighbouring subunit, as supported by previous results<sup>33</sup>. The distance between TM1-TM2 and the cytoplasmic domain in MscS-PC-18:1- $\beta$ CD was about 6.3 Å shorter than that in the open conformation (Extended Data Fig. 6a), almost completely eliminating the hydrophobic pocket. In summary, lipid removal appears to have generated tension in the nanodisc, but as it did not dissipate upon channel opening, MscS transitioned to the desensitized state.

We tested our conclusion that MscS-PC-18:1- $\beta$ CD reflects the desensitized state in two ways. First, we reconstituted MscS into azolectin liposomes and perfused excised patches with  $\beta$ CD (Fig. 2f, g, Extended Data Fig. 6b, c). Within about 60 s,  $\beta$ CD (10 mM) generated MscS activity without application of negative pressure. In patches that did not rupture, the MscS current subsequently declined to baseline, and no further channel activity could be elicited (Fig. 2f), demonstrating that prolonged incubations of membranes with  $\beta$ CD do push embedded MscS channels into the desensitized state. Second, we purified the Gly113Ala MscS mutant, which under membrane tension opens but does not desensitize<sup>18</sup>, reconstituted it into nanodiscs and subjected these to the same  $\beta$ CD treatment that was used for wild-type MscS. Cryo-EM analysis of the MscS(Gly113Ala)-PC-18:1- $\beta$ CD sample did not reveal any classes with a highly tilted TM1-TM2 as seen in MscS-PC-18:1- $\beta$ CD (Extended Data Fig. 7a, b), supporting the notion that the structure of MscS-PC-18:1- $\beta$ CD indeed reflects the desensitized state.

### The open conformation of MscS is dynamic

Cryo-EM analysis of the MscS(Gly113Ala)-PC-18:1- $\beta$ CD did not yield the expected structure of MscS in the open conformation seen by X-ray crystallography<sup>10</sup>. Furthermore, most 2D averages showed a smeared-out TMD (Extended Data Fig. 7a), suggesting that the TMD is highly dynamic in the open state. To test this idea, we reconstituted the MscS Ala106Val mutant, which was used to determine the X-ray structure of the open conformation, into PC-18:1 nanodiscs and analysed

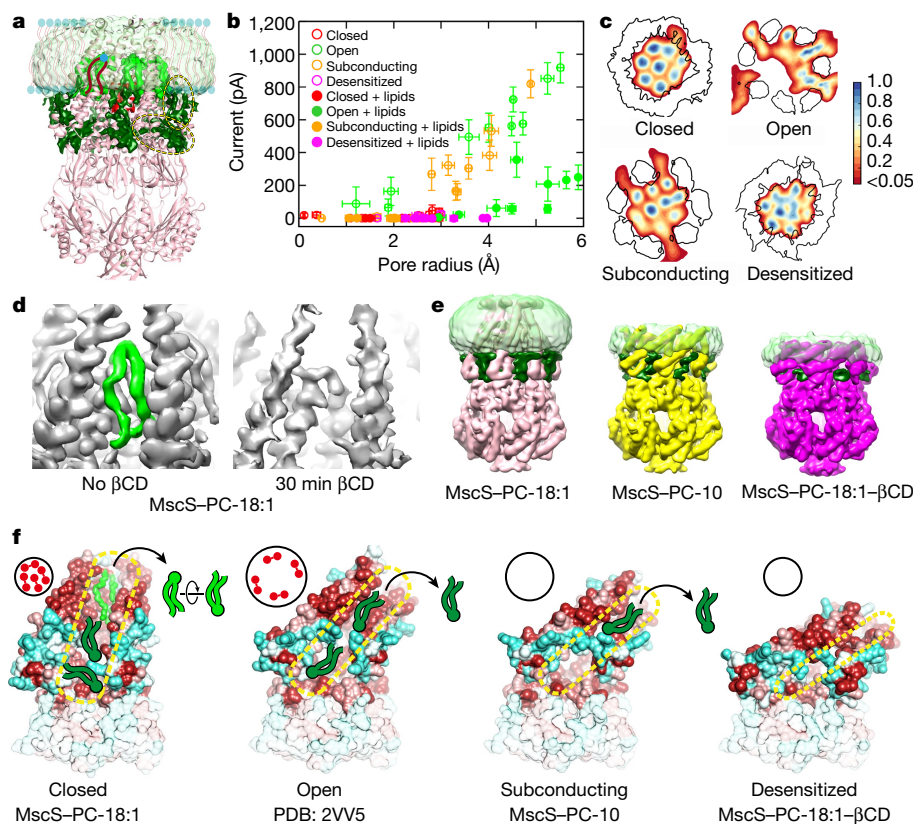


**Fig. 4 | Lipids have diverse roles in the mechanosensation of MscS.**

**a**, Overview of non-protein densities in the MscS-PC-18:1 map. MscS is shown as a pink ribbon, nanodisc as a transparent green surface, and the densities that represent pore lipids, pocket lipids and gatekeeper lipids are shown in red, dark green and light green, respectively. One gatekeeper lipid is shown in cartoon representation and the two densities that represent pocket lipids are circled in yellow. **b**, Ion current as a function of minimum pore radius. The results of the molecular dynamics simulations of MscS in the closed (red), open (green), subconducting (yellow) and desensitized (pink) conformations are shown. Simulations were performed with PC-18:1 lipids in the channel pore (filled circles;  $n = 10, 9, 10$  and  $10$  for closed, open, subconducting and desensitized conformations, respectively) and without PC-18:1 lipids in the channel pore (open circles;  $n = 10, 10, 10$  and  $6$  for closed, open, subconducting and desensitized conformations, respectively). The error bars represent the s.d. of the pore radius (measured with 1-ns frequency) and the s.d. of currents measured in 20-ns windows in each trajectory. **c**, Localization of PC-18:1 lipids inside the MscS channel in molecular dynamics simulations. The densities represent normalized probability distributions for the lipid acyl chains over

the sample by cryo-EM. The 2D averages showed channels with variable TMD thickness (Extended Data Fig. 7c). The averages that showed a thick TMD also displayed clear secondary structure and represented MscS in the closed conformation, which can also be seen in the 3D maps (Extended Data Fig. 7d). However, in averages that showed a thinner TMD, which may represent MscS in the open conformation, the TMD was smeared out and in some classes also asymmetric. None of the 3D maps with a well-defined TMD showed MscS in the open conformation (Fig. 3a, Extended Data Fig. 7c, d). By contrast, cryo-EM analysis of this mutant in the detergent dodecyl maltoside revealed the same open conformation seen in the X-ray structure (Fig. 3b, Extended Data Fig. 7e–g). Finally, to test whether unmodified, wild-type MscS would adopt a defined open conformation in a lipid bilayer, we treated MscS in PC-18:1 nanodiscs with  $\beta$ CD for shorter times. After incubations of 30 min and 4 h, not one of the resulting classes showed MscS in a defined open conformation (Extended Data Fig. 8). Together, these results suggest that, in the context of a lipid bilayer, the conformation of the TMD of MscS in the open state is dynamic.

one simulation trajectory for each conformation. The black lines indicate the densities for the TM3a helices. **d**, The density for the gatekeeper lipid (green) in MscS-PC-18:1 (left) is not seen after a 30-min incubation with  $\beta$ CD (right). The density for TM1 also becomes weaker. **e**, The density in the hydrophobic pocket that represents the mobile pocket lipids (dark green) is largest in the closed state of MscS, smaller in the subconducting state and least in the desensitized state. The density of the nanodisc is shown as a transparent green surface. **f**, The model for the mechanosensation of MscS. In the resting state, the conductance pathway (black circle, top left) is blocked by the pore lipids (red circles). At onset of membrane tension, gatekeeper lipids (light green) are the first to dissociate, allowing MscS to adopt the open conformation. The pore lipids move to the pore periphery, allowing some ion conduction. Sustained membrane tension causes the pore lipids to leave the channel and increasing amounts of pocket lipids (dark green) to leave the hydrophobic pockets (yellow dashed line), which eventually almost completely disappear. The increasing loss of pocket lipids allows the TMD to transition from the open to the subconducting and finally to the desensitized state.

### Role of lipids in MscS mechanosensation

As with two recent structures of MscS in nanodiscs<sup>11,26</sup>, our MscS-PC-18:1 map showed several densities that represent bound lipids, which we named ‘pore’, ‘gatekeeper’ and ‘pocket’ lipids (Fig. 4a).

Eight rod-shaped densities inside the MscS pore ran from the entrance of the periplasmic pore to close to the gating residue Leu105 (Extended Data Fig. 9a, b). We modelled these densities as four pore lipids. We then performed molecular dynamics simulations of MscS in the different conformations (Fig. 4b, c, Supplementary Information). In the closed conformation, the pore lipids were not only stable (Fig. 4c) but also appeared to be required for MscS to be completely impermeable to ions (Fig. 4b, compare the empty and filled red circles). In molecular dynamics simulations of MscS in the open conformation, the pore lipids rapidly moved to the periphery of the pore (Fig. 4c, Supplementary Video 3) and thus allowed some ion conduction, whereas simulations without the pore lipids showed appreciably higher ion conduction (Fig. 4b).

During the 100–200-ns molecular dynamics simulations without field and the subsequent 500-ns simulations with field, all lipids remained inside the channel (Fig. 4c) and we never observed pore lipids leaving the inside of the channel. Although this may simply require longer simulation times and/or conformational dynamics of MscS in the open conformation (see above) that was not captured in the simulations, we cannot conclusively rule out the possibility that the pore lipids remain in the channel during the entire conformational cycle. However, as molecular dynamics simulations showed that in the open conformation the pore lipids substantially reduced ion conduction and completely prevented it in the subconducting conformation (Fig. 4b), and as we did not observe density for the pore lipids in the maps of MscS in the subconducting and desensitized states, we favour a model in which sustained membrane tension causes the pore lipids to leave the channel, facilitated by the dynamic nature of the TMD of MscS in the open conformation.

The best-resolved lipid was located in between the hydrophobic regions of the TM1–TM2 of two neighbouring subunits (Extended Data Fig. 9a–d). While this lipid was located in the cytoplasmic leaflet, it was inverted, so that the headgroup was in the hydrophobic centre of the bilayer (Fig. 4a). This energetically unfavourable headgroup position was stabilized by the hydrophilic environment created by conserved residues Tyr27 and Asn30 on TM1 and Arg88 on TM2 of the neighbouring subunit, where it was shielded from the lipid bilayer (Extended Data Fig. 9c, d). The acyl chains of this lipid are wedged in between the TM1 and TM2 domains and probably stabilize the closed conformation of MscS by making it more difficult for the loosely packed neighbouring TM1–TM2 domains to slide against each other. This idea is supported by our analysis of MscS in PC-18:1 nanodiscs after incubation with  $\beta$ CD for 30 min, in which one class showed MscS in the closed conformation but with this lipid missing and a weaker density for TM1 (Fig. 4d). After incubation with  $\beta$ CD for 4 h, one class showed TM1–TM2 to have a higher tilt, but the channel was still closed (Extended Data Fig. 8e). We named the inverted lipid the gatekeeper lipid, because its dissociation from MscS with membrane tension seems likely to increase the mobility of TM1–TM2 and thus to destabilize the closed conformation. In addition, once the gatekeeper lipid leaves its binding pocket, it has to flip and can no longer reassociate with MscS in the same way, committing the channel to conformational change. Thus, the gatekeeper lipid seems to be a critical element of MscS mechanosensation.

The gatekeeper lipid sits in a hydrophobic pocket between neighbouring subunits that extends into the solvent-exposed region of MscS (Extended Data Fig. 2c). In the map of the closed conformation, this pocket is occupied by density (Fig. 4a). Although not sufficiently well-defined for model building, the size and features of the density are consistent with two lipid molecules, which we named pocket lipids. Our and previous molecular dynamics simulations of MscS in the closed conformation<sup>22</sup> showed that lipids can diffuse into these pockets from the cytoplasmic membrane leaflet (Supplementary Video 4). We found that the pockets in our maps of the closed, subconducting and desensitized conformations contained increasingly less density (Fig. 4e) and became increasingly smaller (Fig. 4f). This finding is corroborated by our molecular dynamics simulations, which showed that lipids often diffused from the cytoplasmic leaflet into the pockets in the closed and open states, but only occasionally in the subconducting state, and never in the desensitized state. On average, each pocket held  $3.3 \pm 0.2$  PC-18:1 lipids in the closed conformation,  $1.5 \pm 0.1$  PC-10 lipids in the open state,  $0.6 \pm 0.1$  PC-10 lipid in the subconducting state and no lipids in the desensitized state (Extended Data Fig. 9e). These results suggest that under sustained membrane tension, increasing amounts of lipid are extracted from the pockets, allowing for the tension-induced successive conformational transitions and lending experimental support to the lipids-move-first molecular model of mechanosensitive channel gating (Supplementary Information). Notably, in the molecular dynamics simulations of the subconducting state, the structural integrity of

MscS increased when we placed a PC-10 lipid into each pocket (the root-mean-square deviations over the molecular dynamics simulations decreased from 4.7 to 4.0 Å for the entire protein and from 3.1 to 2.2 Å for TM3a), suggesting that dissociation of the last lipid due to sustained membrane tension will probably induce the transition to the desensitized conformation.

In the desensitized conformation, the contracted TMD does not match the hydrophobic thickness of the surrounding membrane, which, as membrane tension subsides, provides a driving force for MscS to return to the closed conformation, simply by tilting back TM1–TM2 to its resting position. During this process, as the TMD expands, new lipids could associate with MscS, and the system would be fully reset when new gatekeeper lipids stabilize the resting closed conformation.

In summary, we have shown that nanodiscs can be used to create different membrane environments and we have introduced a generally applicable method to mimic membrane tension (Extended Data Fig. 10, Supplementary Information). This approach allowed us to visualize the entire conformational cycle of MscS during mechanosensation, revealing that MscS-associated lipids have critical roles in this process (Supplementary Videos 5, 6).

## Online content

Any methods, additional references, Nature Research reporting summaries, source data, extended data, supplementary information, acknowledgements, peer review information; details of author contributions and competing interests; and statements of data and code availability are available at <https://doi.org/10.1038/s41586-021-03196-w>.

1. Hamill, O. P. & Martinac, B. Molecular basis of mechanotransduction in living cells. *Physiol. Rev.* **81**, 685–740 (2001).
2. Kung, C. A possible unifying principle for mechanosensation. *Nature* **436**, 647–654 (2005).
3. Katta, S., Krieg, M. & Goodman, M. B. Feeling force: physical and physiological principles enabling sensory mechanotransduction. *Annu. Rev. Cell Dev. Biol.* **31**, 347–371 (2015).
4. Cox, C. D., Bavi, N. & Martinac, B. Biophysical principles of ion-channel-mediated mechanosensory transduction. *Cell Rep.* **29**, 1–12 (2019).
5. Sukharev, S. Purification of the small mechanosensitive channel of *Escherichia coli* (MscS): the subunit structure, conduction, and gating characteristics in liposomes. *Biophys. J.* **83**, 290–298 (2002).
6. Levina, N. et al. Protection of *Escherichia coli* cells against extreme turgor by activation of MscS and MscL mechanosensitive channels: identification of genes required for MscS activity. *EMBO J.* **18**, 1730–1737 (1999).
7. Sukharev, S. I., Blount, P., Martinac, B., Blattner, F. R. & Kung, C. A large-conductance mechanosensitive channel in *E. coli* encoded by *mscL* alone. *Nature* **368**, 265–268 (1994).
8. Martinac, B., Buechner, M., Delcour, A. H., Adler, J. & Kung, C. Pressure-sensitive ion channel in *Escherichia coli*. *Proc. Natl Acad. Sci. USA* **84**, 2297–2301 (1987).
9. Bass, R. B., Strop, P., Barclay, M. & Rees, D. C. Crystal structure of *Escherichia coli* MscS, a voltage-modulated and mechanosensitive channel. *Science* **298**, 1582–1587 (2002).
10. Wang, W. et al. The structure of an open form of an *E. coli* mechanosensitive channel at 3.45 Å resolution. *Science* **321**, 1179–1183 (2008).
11. Reddy, B., Bavi, N., Lu, A., Park, Y. & Perozo, E. Molecular basis of force-from-lipids gating in the mechanosensitive channel MscS. *eLife* **8**, e50486 (2019).
12. Martinac, B. Mechanosensitive ion channels: molecules of mechanotransduction. *J. Cell Sci.* **117**, 2449–2460 (2004).
13. Haswell, E. S., Phillips, R. & Rees, D. C. Mechanosensitive channels: what can they do and how do they do it? *Structure* **19**, 1356–1369 (2011).
14. Booth, I. R. Bacterial mechanosensitive channels: progress towards an understanding of their roles in cell physiology. *Curr. Opin. Microbiol.* **18**, 16–22 (2014).
15. Akitake, B., Anishkin, A. & Sukharev, S. The “dashpot” mechanism of stretch-dependent gating in MscS. *J. Gen. Physiol.* **125**, 143–154 (2005).
16. Cox, C. D. et al. Selectivity mechanism of the mechanosensitive channel MscS revealed by probing channel subconducting states. *Nat. Commun.* **4**, 2137 (2013).
17. Kamaraju, K., Belyy, V., Rowe, I., Anishkin, A. & Sukharev, S. The pathway and spatial scale for MscS inactivation. *J. Gen. Physiol.* **138**, 49–57 (2011).
18. Edwards, M. D., Bartlett, W. & Booth, I. R. Pore mutations of the *Escherichia coli* MscS channel affect desensitization but not ionic preference. *Biophys. J.* **94**, 3003–3013 (2008).
19. Koprrowski, P. & Kubalski, A. Voltage-independent adaptation of mechanosensitive channels in *Escherichia coli* protoplasts. *J. Membr. Biol.* **164**, 253–262 (1998).
20. Pliotas, C. et al. Conformational state of the MscS mechanosensitive channel in solution revealed by pulsed electron-electron double resonance (PELDOR) spectroscopy. *Proc. Natl Acad. Sci. USA* **109**, E2675–E2682 (2012).
21. Lai, J. Y., Poon, Y. S., Kaiser, J. T. & Rees, D. C. Open and shut: crystal structures of the dodecylmaltoside solubilized mechanosensitive channel of small conductance from *Escherichia coli* and *Helicobacter pylori* at 4.4 Å and 4.1 Å resolutions. *Protein Sci.* **22**, 502–509 (2013).

22. Pliotas, C. et al. The role of lipids in mechanosensation. *Nat. Struct. Mol. Biol.* **22**, 991–998 (2015).
  23. Zhang, X. et al. Structure and molecular mechanism of an anion-selective mechanosensitive channel of small conductance. *Proc. Natl Acad. Sci. USA* **109**, 18180–18185 (2012).
  24. Brohawn, S. G., Campbell, E. B. & MacKinnon, R. Physical mechanism for gating and mechanosensitivity of the human TRAAK K<sup>+</sup> channel. *Nature* **516**, 126–130 (2014).
  25. Guo, Y. R. & MacKinnon, R. Structure-based membrane dome mechanism for Piezo1 mechanosensitivity. *eLife* **6**, e33660 (2017).
  26. Rasmussen, T., Flegler, V. J., Rasmussen, A. & Böttcher, B. Structure of the mechanosensitive channel MscS embedded in the membrane bilayer. *J. Mol. Biol.* **431**, 3081–3090 (2019).
  27. Xue, F. et al. Membrane stiffness is one of the key determinants of *E. coli* MscS channel mechanosensitivity. *Biochim. Biophys. Acta Biomembr.* **1862**, 183203 (2020).
  28. Nomura, T. et al. Differential effects of lipids and lyso-lipids on the mechanosensitivity of the mechanosensitive channels MscL and MscS. *Proc. Natl Acad. Sci. USA* **109**, 8770–8775 (2012).
  29. Bavi, N. et al. The role of MscL amphipathic N terminus indicates a blueprint for bilayer-mediated gating of mechanosensitive channels. *Nat. Commun.* **7**, 11984 (2016).
  30. Saotome, K. et al. Structure of the mechanically activated ion channel Piezo1. *Nature* **554**, 481–486 (2018).
  31. Reddy, A. S., Warshaviak, D. T. & Chachivili, M. Effect of membrane tension on the physical properties of DOPC lipid bilayer membrane. *Biochim. Biophys. Acta* **1818**, 2271–2281 (2012).
  32. Lewis, B. A. & Engelman, D. M. Lipid bilayer thickness varies linearly with acyl chain length in fluid phosphatidylcholine vesicles. *J. Mol. Biol.* **166**, 211–217 (1983).
  33. Belyy, V., Anishkin, A., Kamaraju, K., Liu, N. & Sukharev, S. The tension-transmitting ‘clutch’ in the mechanosensitive channel MscS. *Nat. Struct. Mol. Biol.* **17**, 451–458 (2010).
- Publisher’s note** Springer Nature remains neutral with regard to jurisdictional claims in published maps and institutional affiliations.
- © The Author(s), under exclusive licence to Springer Nature Limited 2021

## Methods

### Protein expression and purification

Wild-type, Gly113Ala and Ala106Val mutant *Escherichia coli* MscS were cloned into the pet28-b vector with an N-terminal 6×His tag. The plasmids were used to transform *E. coli* BL21(DE3) cells, which were grown at 37 °C in lysogeny broth medium containing 50 µg/ml kanamycin. When the culture reached an OD<sub>600</sub> of approximately 0.6, protein expression was induced by adding isopropyl β-D-1-thiogalactopyranoside to a final concentration of 1 mM. After another 4 h at 37 °C, cells were collected by centrifugation at 5,000g for 10 min at 4 °C. Cells were resuspended and lysed by sonication in buffer containing 30 mM Tris-HCl, pH 7.5, 250 mM NaCl and 1% Triton-X100, supplemented with one tablet of cOmplete protease inhibitor cocktail (Sigma-Aldrich). The lysate was clarified by centrifugation at 16,000g for 30 min at 4 °C, incubated with 2 ml nickel-affinity resin (Qiagen) and washed with 40 bead volumes of 40 mM imidazole in 30 mM Tris-HCl, pH 7.5, 250 mM NaCl and 0.02% dodecyl maltoside (DDM). Protein was eluted with 250 mM imidazole in 30 mM Tris-HCl, pH 7.5, 150 mM NaCl and 0.02% DDM, concentrated using Amicon Ultra 15-ml 50-kDa cut-off centrifugal filters (Millipore Sigma) and loaded onto a Superdex200 column (GE Healthcare) in 30 mM Tris-HCl, pH 7.5, 150 mM NaCl and 0.02% DDM. Fractions containing MscS were pooled and used immediately for reconstitution into nanodiscs.

The membrane scaffold protein (MSP) used in this study was MSP1E3D1, which assembles nanodiscs of 13 nm in diameter. MSP1E3D1 with a tobacco etch virus (TEV) protease-cleavable N-terminal 6×His tag was expressed in *E. coli* BL21(DE3) cells as described for MscS. The cells were lysed by sonication in 30 mM Tris-HCl, pH 7.5, 500 mM NaCl and 1% Triton-X100, supplemented with one tablet of cOmplete protease inhibitor cocktail (Sigma-Aldrich). After centrifugation at 16,000g for 30 min at 4 °C, the supernatant was loaded onto a nickel-affinity column, and the beads were washed with 20 column volumes of 40 mM imidazole in 30 mM Tris-HCl, pH 7.5, 500 mM NaCl and 1% sodium cholate, followed by 20 column volumes of the same buffer without sodium cholate. Protein was eluted with 250 mM imidazole in 30 mM Tris-HCl, pH 7.5, and 150 mM NaCl. The His tag was removed by incubation with TEV protease at a molar MSP1E3D1:TEV protease ratio of 30:1. After dialysis overnight at 4 °C against 400 ml 30 mM Tris-HCl, pH 7.5, and 150 mM NaCl, the sample was loaded onto a nickel-affinity column to remove the cleaved-off His tag and the His-tagged TEV protease. The flow-through was concentrated using Amicon Ultra 15-ml 10-kDa cut-off centrifugal filters (Millipore Sigma) and loaded onto a Superdex200 column equilibrated with 30 mM Tris-HCl, pH 7.5, and 150 mM NaCl. The MSP1E3D1-containing fractions were pooled and concentrated to 4.2 mg/ml using Amicon Ultra 15-ml 10-kDa cut-off centrifugal filters (Millipore Sigma).

### Reconstitution of MscS into nanodiscs

All lipids were purchased from Avanti Polar Lipids and solubilized with 20 mM sodium cholate in 30 mM Tris-HCl, pH 7.5, and 150 mM NaCl with sonication. MscS and MSP1E3D1 were mixed with the desired detergent-solubilized lipid at a molar ratio of 1:10:1,000 in 12 ml of 30 mM Tris-HCl, pH 7.5, 150 mM NaCl and 0.02% DDM. After 10 min, 1.5 ml of Bio-Beads SM-2 slurry (Bio-Rad) was added to remove the detergents. After overnight incubation with constant rotation, the Bio-Beads were allowed to settle by gravity. The supernatant was loaded onto a nickel-affinity column to remove the empty nanodiscs. The column was washed with 20 column volumes of 40 mM imidazole in 30 mM Tris-HCl, pH 7.5, and 150 mM NaCl, and MscS reconstituted into nanodiscs was eluted with 250 mM imidazole in 30 mM Tris-HCl, pH 7.5, and 150 mM NaCl. Samples were concentrated using Amicon Ultra 15-ml 50-kDa cut-off centrifugal filters (Millipore Sigma) and loaded onto a Superdex200 column equilibrated with 30 mM Tris-HCl, pH 7.5, and 150 mM NaCl. Peak fractions containing MscS in nanodiscs were pooled and used to prepare vitrified samples for cryo-EM.

### Treatment of MscS-containing nanodiscs with βCD

To test whether βCD (332615, Sigma-Aldrich) can extract lipids from nanodiscs, empty PC-18:1 nanodiscs were incubated with 0 mM, 10 mM and 100 mM βCD for 2 h and 16 h. Whereas nanodiscs that were incubated for 16 h without βCD remained intact, no nanodiscs remained after incubation with 100 mM βCD. This concentration was thus used to incubate PC-18:1 nanodiscs containing MscS with βCD. After 16 h, the sample showed substantial aggregation, but intact nanodiscs could be isolated by size-exclusion chromatography on a Superdex200 column equilibrated with 30 mM Tris-HCl, pH 7.5, and 150 mM NaCl (Extended Data Fig. 4b). The peak fractions were pooled, concentrated using Amicon Ultra 4-ml 50-kDa cut-off centrifugal filters (Millipore Sigma) and used immediately for cryo-EM sample preparation. The same procedure was also used for βCD treatment of PC-18:1 nanodiscs containing MscS for 30 min and 4 h, as well as PC-18:1 nanodiscs containing Gly113Ala mutant MscS for 16 h.

### EM specimen preparation and data collection

The homogeneity of all samples was first examined by negative-stain EM with 0.7% (w/v) uranyl formate as previously described<sup>34</sup>.

For cryo-EM, the protein concentration was measured with a NanoDrop spectrophotometer (Thermo Fisher Scientific) and adjusted to 0.05 mg/ml. A thin layer of homemade continuous carbon film was deposited onto 300 mesh R1.2/1.3 Cu grids (Quantifoil) to minimize preferred orientations. Aliquots of 4 µl were applied to glow-discharged grids using a Vitrobot Mark VI (Thermo Fisher Scientific) set at 4 °C and 100% humidity. After 20 s, grids were blotted for 0.5 s with a blot force of -2 and plunged into liquid nitrogen-cooled ethane.

Cryo-EM imaging was performed in the Cryo-EM Resource Center at the Rockefeller University using SerialEM<sup>35</sup>. Data collection parameters are summarized in Extended Data Table 1.

For MscS-PC-14, MscS-PC-12 and MscS-PC-11, data were collected on a 200-kV Talos Arctica electron microscope (Thermo Fisher Scientific) at a nominal magnification of ×22,500, corresponding to a calibrated pixel size of 1.5 Å on the specimen level. Images were collected using a defocus range from -1.5 to -3 µm with a K2 Summit direct electron detector (Gatan) in super-resolution counting mode. Exposures of 10 s were dose-fractionated into 40 frames (250 ms per frame) with a dose rate of 8 electrons/pixel/s (approximately 0.89 electrons per Å<sup>2</sup> per frame), resulting in a total dose of 35 electrons per Å<sup>2</sup>.

For MscS in PC-10 nanodiscs and DDM-solubilized Ala106Val mutant MscS, data were collected on a 300-kV Titan Krios electron microscope (Thermo Fisher Scientific) at a nominal magnification of ×22,500, corresponding to a calibrated pixel size of 1.3 Å on the specimen level. Images were recorded using a defocus range from -1.2 to -2.5 µm with a K2 Summit direct electron detector in super-resolution counting mode. Exposures of 10 s were dose-fractionated into 40 frames (250 ms per frame) with a dose rate of 8 electrons per pixel per s (approximately 1.18 electrons per Å<sup>2</sup> per frame), resulting in a total dose of 47 electrons per Å<sup>2</sup>.

For wild-type and Ala106Val mutant MscS in PC-18:1 nanodiscs and nanodisc samples treated with βCD, data were collected on a 300-kV Titan Krios electron microscope at a nominal magnification of ×28,000, corresponding to a calibrated pixel size of 1.0 Å on the specimen level. Images were collected using a defocus range of -1.2 to -2.5 µm with a K2 Summit direct electron detector in super-resolution counting mode. The 'superfast mode' in SerialEM was used, in which 3 × 3 holes are exposed using beam tilt and image shift before moving the stage to the next position<sup>36</sup>. Exposures of 10 s were dose-fractionated into 40 frames (250 ms per frame) with a dose rate of 6 electrons per pixel per s (approximately 1.38 electrons per Å<sup>2</sup> per frame), resulting in a total dose of 55 electrons per Å<sup>2</sup>.

### Image processing

For all samples, the collected movie stacks were gain-normalized, motion-corrected, dose-weighted and binned over  $2 \times 2$  pixels in Motioncorr<sup>37</sup>. The contrast transfer function (CTF) parameters were determined with CTFFIND4<sup>38</sup> implemented in RELION-3<sup>39</sup>. Particles were automatically picked with Gautomatch (<http://www.mrc-lmb.cam.ac.uk/kzhang/Gautomatch/>), extracted into individual images, normalized and subjected to 2D classification in RELION-3, which was used for all further processing steps. Particles from 2D classes that showed clear secondary structural features were combined and subjected to 3D classification. Particles in 3D classes that showed well-defined TMDs were combined and subjected to another round of 3D classification (this step was omitted for the datasets of MscS(Gly113Ala)-PC-18:1- $\beta$ CD, MscS-PC-18:1- $\beta$ CD(30 min), MscS-PC-18:1- $\beta$ CD(4 h), MscS(Ala106Val)-PC-18:1 and Ala106Val mutant MscS in DDM). Particles from classes that showed well-defined and similar TMDs were combined and centred by re-extraction. The orientation parameters of the re-extracted particles were further refined, and the resulting density maps were sharpened by post-processing. For the datasets collected on the Titan Krios, namely, MscS-PC-18:1 (Extended Data Fig. 1c–e), MscS-PC-10 (Extended Data Fig. 3) and MscS-PC-18:1- $\beta$ CD (Extended Data Fig. 4c–e), CTF refinement and Bayesian polishing were performed<sup>40</sup>. Fourier shell correlation (FSC) curves, local resolution maps and resolution-filtered maps were calculated in RELION-3 (Extended Data Fig. 5).

### Model building and refinement

Atomic models were built into the three high-resolution maps of MscS-PC-18:1, MscS-PC-10 and MscS-PC-18:1- $\beta$ CD using, as starting models, the crystal structures of MscS in the closed state (PDB: 2OAU) and the open state (PDB: 2VV5), and the model of residues 15–27 generated with I-TASSER<sup>41</sup>. The model for the PC-18:1 lipid was taken from PDB: 6CCH, with restraints generated in Phenix<sup>42</sup>. The cytoplasmic domains and TMDs were placed separately into the cryo-EM maps by rigid-body fitting in UCSF Chimera<sup>43</sup>. The residues in all models except for TM1–TM2 of MscS-PC-18:1- $\beta$ CD were fit manually and adjusted in Coot<sup>44</sup>. The models were improved by iterative cycles of refinement with phenix.real\_space\_refine and manual adjustment in Coot. The models were refined against half map 1, and FSC curves were then calculated between the refined model and half map 1 (work), half map 2 (free) and the combined map (Extended Data Fig. 5b).

### Molecular dynamics simulations

We conducted molecular dynamics simulations of MscS in the closed, open, subconducting and desensitized states using the GROMACS2019 software package<sup>45</sup> and the CHARMM36m force field<sup>46</sup>. The CHARMM-GUI web server<sup>47</sup> was used to assemble the simulation systems, which contained one MscS channel, approximately 300 lipids, about 20,000–25,000 water molecules and roughly 800–1,000 potassium and chloride ions. We used PC-18:1 lipids for simulations of MscS in the closed conformation and PC-10 lipids for simulations of MscS in the open, subconducting and desensitized conformations, owing to the different thickness of the hydrophobic region of MscS in the different conformations. Only the TMD of MscS was used in the molecular dynamics simulations. The potassium concentration was 1 mol/l for all systems. Each system was first equilibrated for 100–200 ns during which time restraints on the water molecules, lipids and protein were gradually removed. Ten parallel simulations without any restraints were then conducted for 100–200 ns without any external field. An integration timestep of 2 fs was used, and the LINCS algorithm<sup>48</sup> was applied to constrain all the hydrogen-containing bonds. We used the Particle Mesh Ewald method<sup>49,50</sup> to calculate the long-range electrostatic interactions, with a Fourier grid spacing of 0.12 nm, an interpolation order of 4 for the Ewald mesh, and a cut-off value of 1.2 nm. The van der Waals interactions were turned off from 1.0 to 1.2 nm using the force

switch method<sup>51</sup>. The semi-isotropic Parrinello–Rahman barostat<sup>52,53</sup> and the Nosé–Hoover thermostat<sup>54,55</sup> were used to maintain the pressure and temperature at 1 bar and 303 K, respectively.

We studied the behaviour of the lipids associated with MscS. The gatekeeper lipids were included in our simulations of MscS in the closed conformation and stayed stably in position for the duration of the simulations.

To study the behaviour of the pore lipids inside the channel, four PC-18:1 lipids were placed close to the extracellular entrance of the MscS channel in the different conformations with the acyl chains pointing to the channel pore. An external force was applied on the lipid acyl chains for 10 ps to pull them towards the channel pore. The systems were subjected to the above protocol for equilibrium and production simulations. The density maps describing the distribution of the lipid acyl chains integrated over the course of one production simulation for each of the MscS conformations were calculated by using the densmap tool of the GROMACS2019 package. The trajectories were first superimposed on the basis of the backbone atoms of the TM3a helices, and the probability distributions of the positions of the atoms of the lipid tails were then averaged over the duration of the simulations. The results were normalized relative to the maximum distribution probability (that is, the probability values were divided by the maximum value).

During the equilibration phase of all molecular dynamics simulations of MscS in the closed and open conformation and occasionally also for MscS in the subconducting conformation, lipids spontaneously diffused into the solvent-exposed regions of the hydrophobic pockets between adjacent subunits and stayed there for the duration of the production runs. To count the number of lipids that occupy these pockets, we calculated the distance between the centres of mass (COMs) of the lipid acyl chains in the cytoplasmic leaflet and the COMs of the TM3a helices. A lipid acyl chain was considered to be located in a hydrophobic pocket if the distance of its COM from the COM of the closest TM3a helix was smaller than a cut-off value, which was defined as the average of the distances between the COMs of the cytoplasmic half of each TM1 helix and the COMs of the TM3a helices projected onto the membrane plane. Each lipid acyl chain was counted as half a lipid. This analysis was performed with in-house written Python scripts and using the MDAnalysis library<sup>56</sup>.

To investigate ion conduction of MscS in different conformations, production simulations were continued for another 500 ns with a constant electrostatic field<sup>57</sup> applied to mimic a transmembrane voltage of approximately 340 mV. Pore radii were calculated for these simulations by extracting 100 equidistant frames and determining the minimal pore radii using the program HOLE<sup>58</sup> and a grid spacing of 0.25 Å. The reported value for each simulation is the average over the 100 individual measurements from the analysed trajectory. To count ion permeation events, a buffer region was defined that approximately corresponded to the thickness of the membrane. An ion permeation event was defined as the transfer of a potassium or chloride ion from one side of the buffer region to the other (not counting ion transfers across the periodic boundaries). MscS in the subconducting state without any pocket lipids did not conduct ions (not shown) and the protein conformation was not stable (the root-mean-square deviations of the backbone atoms over the course of the simulation were 4.7 Å for the entire protein and 3.1 Å for TM3a helices). We found that the presence of a pocket lipid stabilized the conformation. To accomplish this, we selected a lipid in the vicinity of the pocket and applied an external force on the lipid tails until the lipid entered the pocket, which took no more than 20 ps. The presence of a PC-10 lipid in the solvent-exposed region of each of the hydrophobic pockets stabilized the protein (the root-mean-square deviations were 4.0 Å for the entire protein and 2.2 Å for TM3a helices), allowing us to measure the values for ion conduction of the subconducting state given in Fig. 4b.

In 8 of the 80 single trajectories, we observed spontaneous formation of a pore in the membrane, which we consider to be a computational

artefact, possibly caused by the short lipid tails of only 10 carbon atoms (pore formation was never observed in simulations using PC-18:1 lipids). For these eight trajectories, we only analysed the portion of the trajectories before pore formation occurred. As a proxy for pore formation, we used phosphorus–phosphorus contacts between lipid headgroups and a cut-off of 0.8 nm. Pore formation was deemed to have started once the moving average over 10 ns dropped below the equilibrium value minus one standard deviation. The membrane was intact in 92.2% of our trajectories (amounting to 36.9  $\mu$ s). Of note, the conclusions drawn from our simulations remained qualitatively unchanged if we discarded the entire trajectories in which pore formation occurred.

To assess how removing lipids from a bilayer affects membrane tension, we conducted molecular dynamics simulations of a bilayer containing 200 PC-18:1 lipids. In these simulations, we fixed the  $x$  and  $y$  dimensions of the membrane (that is, the area of the bilayer) at the equilibrium value of the initial system and gradually removed lipids from the bilayer. Specifically, we removed two lipids from each leaflet at a time, which was followed by 5-ns equilibrium simulations, during which time the membrane tension was assessed, before removing the next four lipids. Simulations of some of the systems (the percentage of removed lipids ranged from 2% to 40%) were extended to 1.0  $\mu$ s, and the last 0.5  $\mu$ s trajectories were used to calculate the membrane tension.

### MscS channel reconstitution and patch-clamp electrophysiology

MscS was reconstituted into soy polar azolectin (Avanti) liposomes, a lipid mixture that was found to be most suitable for electrophysiological studies on MscS, at a protein-to-lipid ratio of 1:200 using the dehydration–rehydration (D/R) method<sup>59</sup>. Soy polar azolectin was dissolved in chloroform and dried under nitrogen flow. The lipid film was then suspended in D/R buffer (5 mM HEPES, pH 7.2 (adjusted with KOH), and 200 mM KCl) and vortexed, followed by sonication in a water bath for 20 min. MscS was added into the lipid mixture at a ratio of 1:200 (w:w) and incubated for 3 h at room temperature with agitation. Then, 300 mg of Bio-Beads SM2 (Bio-Rad) was added. After 3 h, the mixture was centrifuged at 40,000 rpm for 40 min at room temperature, and the lipid mixture was desiccated overnight.

For patch-clamp measurements, the proteoliposomes were rehydrated in D/R buffer for 6 h or overnight before use. The bath and pipette recording solutions used for patch-clamp experiments were the same, consisting of 5 mM HEPES, pH 7.2 (adjusted with KOH), 200 mM KCl and 40 mM MgCl<sub>2</sub>. The current was amplified with an Axopatch 200B amplifier (Molecular Devices), filtered at 2 kHz and the data acquired at 10 kHz with a Digidata 1440A interface using pCLAMP 10 acquisition software (Molecular Devices). Negative hydrostatic pressure was applied to the patch pipette using a high-speed pressure clamp (HSPC-1; ALA Scientific Instruments). The open probability ( $P_o$ ) was determined as the number of open channels over the total number of channels in the patch determined at saturating pressure.

### Measuring the diameter of MscS-containing nanodiscs

After 2D classification of the MscS–PC-18:1 and MscS–PC-18:1– $\beta$ CD datasets in RELION-3, classes showing side views of MscS in nanodiscs were combined, yielding 73,646 and 74,499 particles, respectively. The particles were re-centred and the particle images were phase-flipped, rescaled to 64  $\times$  64 pixels, and subjected to 2D classification with the iterative stable alignment and clustering (ISAC) algorithm<sup>60</sup> specifying 500 images per group and a pixel error threshold of 0.7. After 4 and 3 generations, 175 and 166 averages were generated for the samples before and after  $\beta$ CD treatment, respectively. We wrote scripts in SPIDER<sup>61</sup> to measure the diameter of the nanodiscs in the class averages in an unbiased manner. In brief, the averages were first oriented so that the symmetry axis of MscS was aligned with the  $y$  axis. A density threshold was then chosen to select mostly background pixels, which were set to zero. Some remaining background regions were identified based on

the number of connected pixels, which were then also set to zero. The top half of the particle images, which contained the nanodiscs, were windowed out and projected onto the  $x$  axis, resulting in each particle image being represented by a single line. The distances between the first and last non-zero pixels in each line were read out as the diameters of the nanodiscs. The results were confirmed by visual inspection.

### Measuring the removal of lipids from nanodiscs by $\beta$ CD using Cy5-labelled lipids

Unlabelled PC-18:1 and Cy5-labelled PC-18:1 (Avanti Polar Lipids) in chloroform were mixed at a molar ratio of 17:1. The lipid mixture was dried under argon gas and kept under vacuum overnight. The lipid mixture was then used to reconstitute MscS into nanodiscs and the nanodiscs were treated with  $\beta$ CD as described. Gel-filtration peak fractions before and after  $\beta$ CD treatment were adjusted to a similar protein concentration (0.7–1 mg/ml), and light absorptions at 280 and 650 nm were measured with a NanoDrop spectrophotometer (Thermo Fisher Scientific). Each sample was measured five times and the averaged A650:A280 ratio was used as the Cy5-lipid-to-protein ratio. Three independent experiments were performed.

### Reporting summary

Further information on research design is available in the Nature Research Reporting Summary linked to this paper.

### Data availability

The cryo-EM maps have been deposited in the Electron Microscopy Data Bank under accession codes EMD-21462 (MscS–PC-18:1), EMD-21463 (MscS–PC-10), EMD-21464 (MscS–PC-18:1– $\beta$ CD), EMD-21465 (MscS–PC-18:1– $\beta$ CD-30 min) and EMD-21466 (MscS(Ala106Val)–DDM). The atomic coordinates have been deposited in the PDB under accession codes 6VYK (MscS–PC-18:1), 6VYL (MscS–PC-10) and 6VYM (MscS–PC-18:1– $\beta$ CD).

### Code availability

The custom-written SPIDER scripts used to measure the nanodisc size and the Python codes used to analyse molecular dynamics trajectories are available from the corresponding author on request.

- Ohi, M., Li, Y., Cheng, Y. & Walz, T. Negative staining and image classification — powerful tools in modern electron microscopy. *Biol. Proced. Online* **6**, 23–34 (2004).
- Mastrorade, D. N. Automated electron microscope tomography using robust prediction of specimen movements. *J. Struct. Biol.* **152**, 36–51 (2005).
- Cheng, A. et al. High resolution single particle cryo-electron microscopy using beam-image shift. *J. Struct. Biol.* **204**, 270–275 (2018).
- Zheng, S. Q. et al. MotionCor2: anisotropic correction of beam-induced motion for improved cryo-electron microscopy. *Nat. Methods* **14**, 331–332 (2017).
- Rohou, A. & Grigorieff, N. CTFFIND4: fast and accurate defocus estimation from electron micrographs. *J. Struct. Biol.* **192**, 216–221 (2015).
- Zivanov, J. et al. New tools for automated high-resolution cryo-EM structure determination in RELION-3. *eLife* **7**, e42166 (2018).
- Zivanov, J., Nakane, T. & Scheres, S. H. W. A Bayesian approach to beam-induced motion correction in cryo-EM single-particle analysis. *IUCr* **6**, 5–17 (2019).
- Zhang, Y. I-TASSER server for protein 3D structure prediction. *BMC Bioinformatics* **9**, 40 (2008).
- Adams, P. D. et al. PHENIX: a comprehensive Python-based system for macromolecular structure solution. *Acta Crystallogr. D* **66**, 213–221 (2010).
- Pettersen, E. F. et al. UCSF Chimera—a visualization system for exploratory research and analysis. *J. Comput. Chem.* **25**, 1605–1612 (2004).
- Emsley, P., Lohkamp, B., Scott, W. G. & Cowtan, K. Features and development of Coot. *Acta Crystallogr. D* **66**, 486–501 (2010).
- Abraham, M. J. et al. GROMACS: high performance molecular simulations through multi-level parallelism from laptops to supercomputers. *SoftwareX* **1–2**, 19–25 (2015).
- Huang, J. et al. CHARMM36m: an improved force field for folded and intrinsically disordered proteins. *Nat. Methods* **14**, 71–73 (2017).
- Jo, S., Kim, T. & Im, W. Automated builder and database of protein/membrane complexes for molecular dynamics simulations. *PLoS ONE* **2**, e880 (2007).
- Hess, B., Bekker, H., Berendsen, H. J. C. & Fraaije, J. G. E. M. LINCS: a linear constraint solver for molecular simulations. *J. Comput. Chem.* **18**, 1463–1472 (1997).
- Essmann, U. et al. A smooth particle mesh Ewald method. *J. Chem. Phys.* **103**, 8577–8593 (1995).

50. Darden, T., York, D. & Pedersen, L. Particle mesh Ewald: an  $N \cdot \log(N)$  method for Ewald sums in large systems. *J. Chem. Phys.* **98**, 10089–10092 (1993).
51. Steinbach, P. J. & Brooks, B. R. New spherical-cutoff methods for long-range forces in macromolecular simulation. *J. Comput. Chem.* **15**, 667–683 (1994).
52. Nosé, S. & Klein, M. L. Constant pressure molecular-dynamics for molecular-systems. *Mol. Phys.* **50**, 1055–1076 (1983).
53. Parrinello, M. & Rahman, A. Polymorphic transitions in single-crystals — a new molecular-dynamics method. *J. Appl. Phys.* **52**, 7182–7190 (1981).
54. Hoover, W. G. Canonical dynamics: equilibrium phase-space distributions. *Phys. Rev. A Gen. Phys.* **31**, 1695–1697 (1985).
55. Nosé, S. A molecular-dynamics method for simulations in the canonical ensemble. *Mol. Phys.* **52**, 255–268 (1984).
56. Michaud-Agrawal, N., Denning, E. J., Woolf, T. B. & Beckstein, O. MDAAnalysis: a toolkit for the analysis of molecular dynamics simulations. *J. Comput. Chem.* **32**, 2319–2327 (2011).
57. Roux, B. The membrane potential and its representation by a constant electric field in computer simulations. *Biophys. J.* **95**, 4205–4216 (2008).
58. Smart, O. S., Neduvellil, J. G., Wang, X., Wallace, B. A. & Sansom, M. S. HOLE: a program for the analysis of the pore dimensions of ion channel structural models. *J. Mol. Graph.* **14**, 354–360 (1996).
59. Delcour, A. H., Martinac, B., Adler, J. & Kung, C. Modified reconstitution method used in patch-clamp studies of *Escherichia coli* ion channels. *Biophys. J.* **56**, 631–636 (1989).
60. Yang, Z., Fang, J., Chittuluru, J., Asturias, F. J. & Penczek, P. A. Iterative stable alignment and clustering of 2D transmission electron microscope images. *Structure* **20**, 237–247 (2012).
61. Frank, J. et al. SPIDER and WEB: processing and visualization of images in 3D electron microscopy and related fields. *J. Struct. Biol.* **116**, 190–199 (1996).
62. Buchan, D. W. A., Minneci, F., Nugent, T. C. O., Bryson, K. & Jones, D. T. Scalable web services for the PSIPRED protein analysis workbench. *Nucleic Acids Res.* **41**, W349–W357 (2013).

**Acknowledgements** We thank D. Rees for critical reading of the manuscript, and M. Ebrahim, J. Sotiris and H. Ng at the Evelyn Gruss Lipper Cryo-EM Resource Center of The Rockefeller University for assistance with data collection. We acknowledge the German Research Foundation DFG (SFB 803, Project A03; to B.d.L.G. and C.D.) and the Alexander von Humboldt foundation (to R.-X.G.) for funding. B.M. is supported by a National Health and Medical Research Council of Australia Principal Research Fellowship (APP1135974). C.D.C. is supported by an NSW Health EMCR Fellowship.

**Author contributions** Y.Z. performed the biochemistry and EM experiments. C.D. and R.-X.G. performed the molecular dynamics experiments. B.d.L.G. supervised the molecular dynamics experiments. C.D.C. and B.M. performed the patch-clamp experiments. T.W. conceived and supervised the project. Y.Z., C.D., R.-X.G., C.D.C., B.M., B.d.L.G. and T.W. analysed the results and wrote the manuscript.

**Competing interests** The authors declare no competing interests.

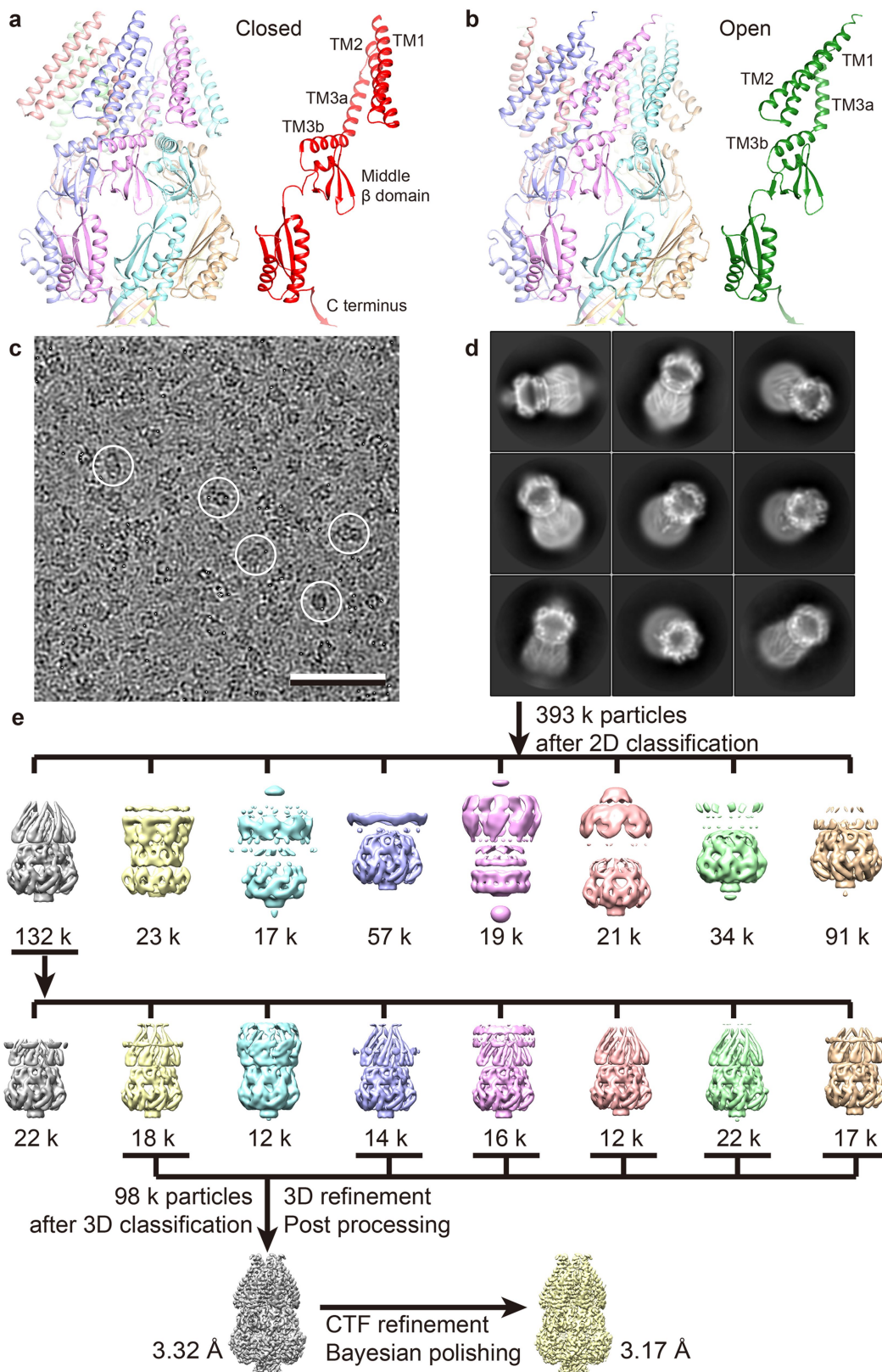
**Additional information**

**Supplementary information** The online version contains supplementary material available at <https://doi.org/10.1038/s41586-021-03196-w>.

**Correspondence and requests for materials** should be addressed to T.W.

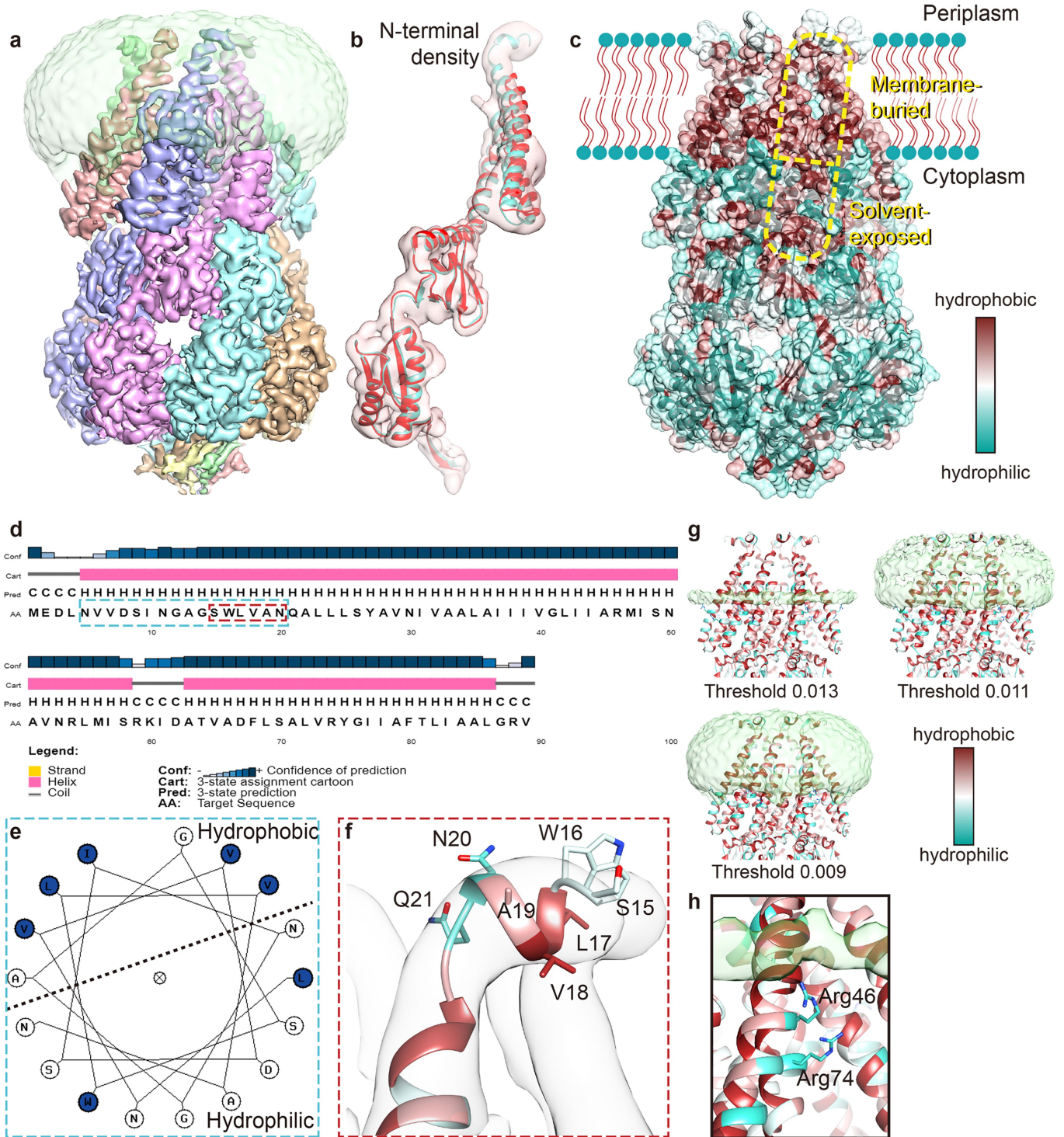
**Peer review information** *Nature* thanks the anonymous reviewer(s) for their contribution to the peer review of this work.

**Reprints and permissions information** is available at <http://www.nature.com/reprints>.



**Extended Data Fig. 1 | Architecture of MscS in the closed and open states and image processing of MscS in PC-18:1 nanodiscs.** **a, b**, Crystal structures of MscS in the closed conformation (PDB: 2OAU) (**a**) and in the open conformation (PDB: 2VV5) (**b**). Left panels: ribbon representation of the channel with each subunit shown in a different colour. Right panels: a single subunit with domains labelled. Opening of the channel is accompanied by an

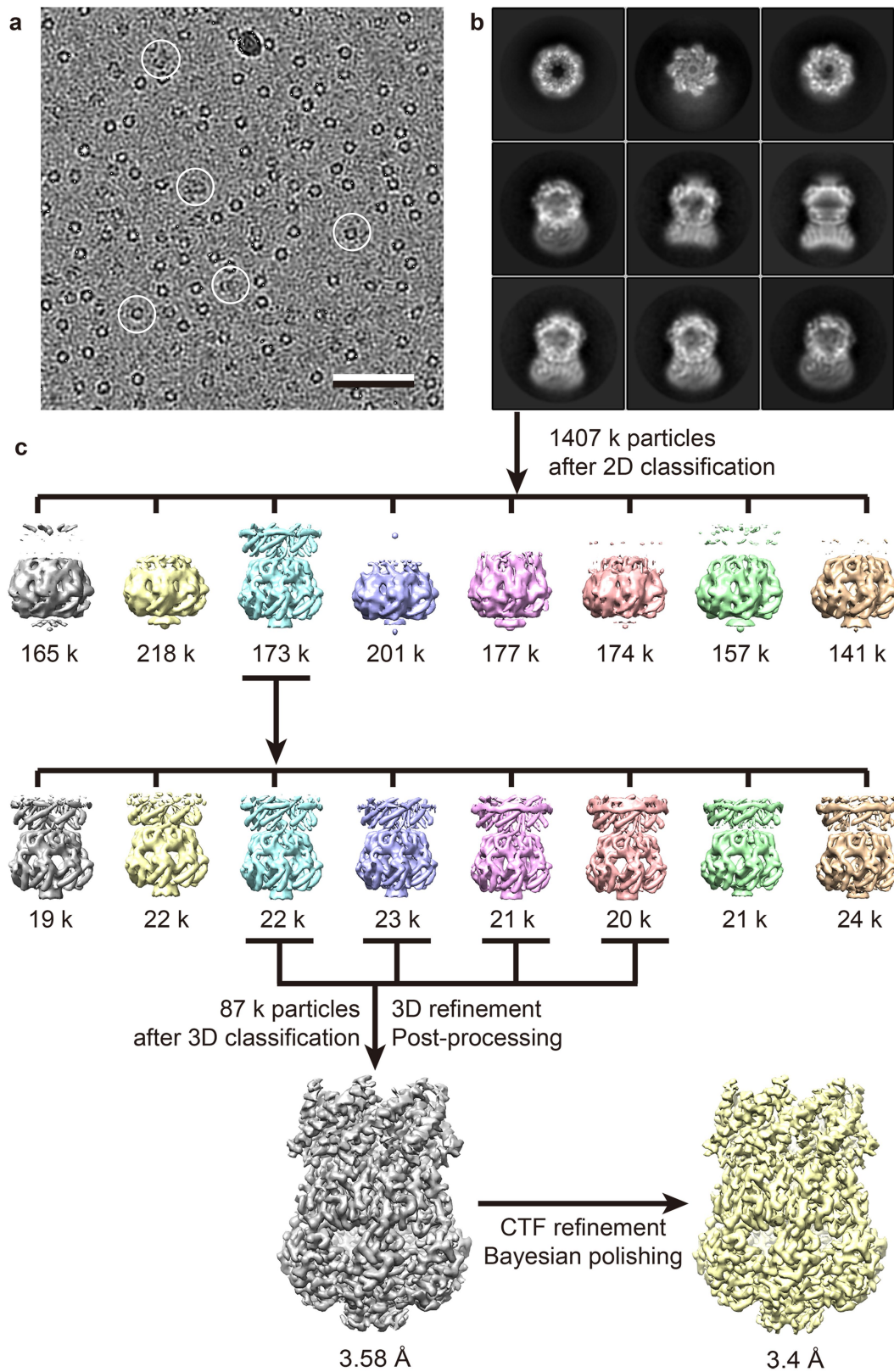
increase in the tilt of TM1–TM2 and a rotation about the symmetry axis. **c**, Area of an image of a vitrified sample. Some particles are circled. Scale bar, 50 nm. **d**, Selected 2D-class averages obtained with RELION-3. Side length of individual averages, 21.6 nm. **e**, Image-processing workflow for 3D classification and refinement in RELION-3 that resulted in a density map at 3.2 Å resolution. See Methods and Extended Data Table 1 for details.



Extended Data Fig. 2 | See next page for caption.

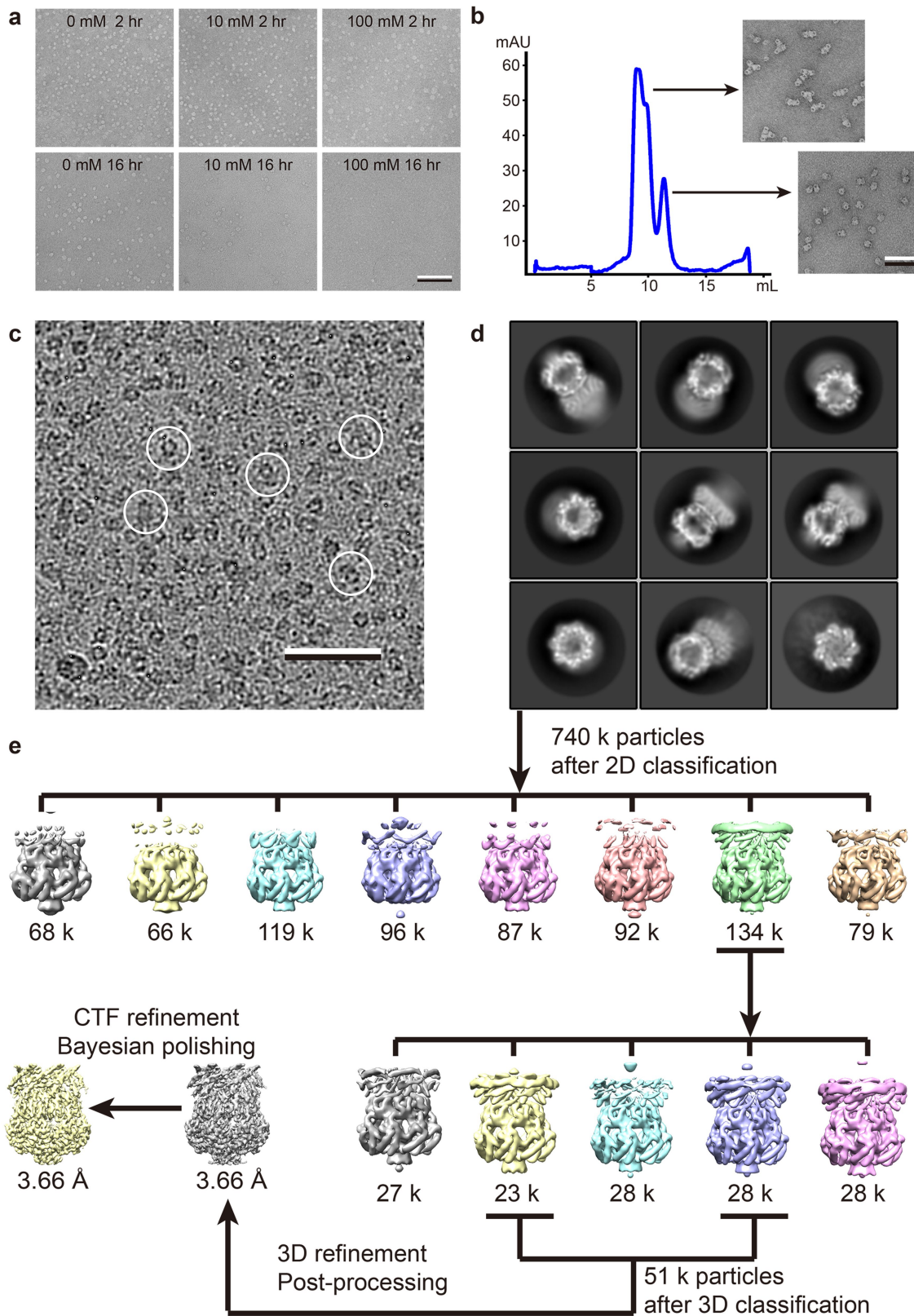
**Extended Data Fig. 2 | Cryo-EM structure of nanodisc-embedded MscS in the closed conformation.** **a**, Cryo-EM map of MscS in a nanodisc formed with PC-18:1. Subunits are coloured as in Extended Data Fig. 1a and nanodisc density is shown as transparent green surface. **b**, Density representing one subunit of MscS-PC-18:1 filtered to 5-Å resolution (transparent red surface) with the atomic model built into it (cyan) and the crystal structure of MscS in the closed conformation (PDB: 2OAU; red). **c**, Hydrophobicity surface map of MscS-PC-18:1 with the model displayed as ribbon. TM1-TM2 and TM3b form a hydrophobic pocket that consists of membrane-buried and solvent-exposed regions (yellow dashed box). **d**, Secondary structure probabilities for MscS residues 1-89 as predicted by PSIPRED<sup>62</sup>. Residues with a high propensity to form  $\alpha$ -helical secondary structure are labelled with 'H' and a pink bar on top. The grey level of the bar above indicates the confidence level of the prediction. **e**, Helical wheel for N-terminal MscS residues 5-20 calculated with Helixator ([http://www.tcdb.org/progs/helical\\_wheel.php](http://www.tcdb.org/progs/helical_wheel.php)). Most hydrophobic residues locate to the upper half of the wheel, while most hydrophilic residues locate to

its lower half. **f**, The density in the MscS-PC-18:1 map representing the N-terminal segment and the model built into the map. Residue Gln21 forms a break between the end of the amphipathic helix and the beginning of TM1. **g**, The nanodisc density (green transparent surface) shown at different contouring levels. The MscS structure is shown in ribbon representation and is coloured according to hydrophobicity. At a high contouring threshold (0.013), the nanodisc density is reduced to a thin belt at the cytoplasmic bilayer boundary. No such belt is seen at the periplasmic bilayer boundary. Furthermore, the cytoplasmic bilayer boundary remains largely stationary with decreasing threshold levels, whereas the periplasmic bilayer boundary moves further out as more density is included. These observations suggest that the positively charged residues Arg46 and Arg74 may interact with the lipid headgroups of the cytoplasmic leaflet and define/stabilize the position of this leaflet. **h**, Close-up view of the location of Arg46 and Arg74 with respect to the nanodisc density contoured at 0.013. The side chains of Arg46 and Arg74 are shown in stick representation.



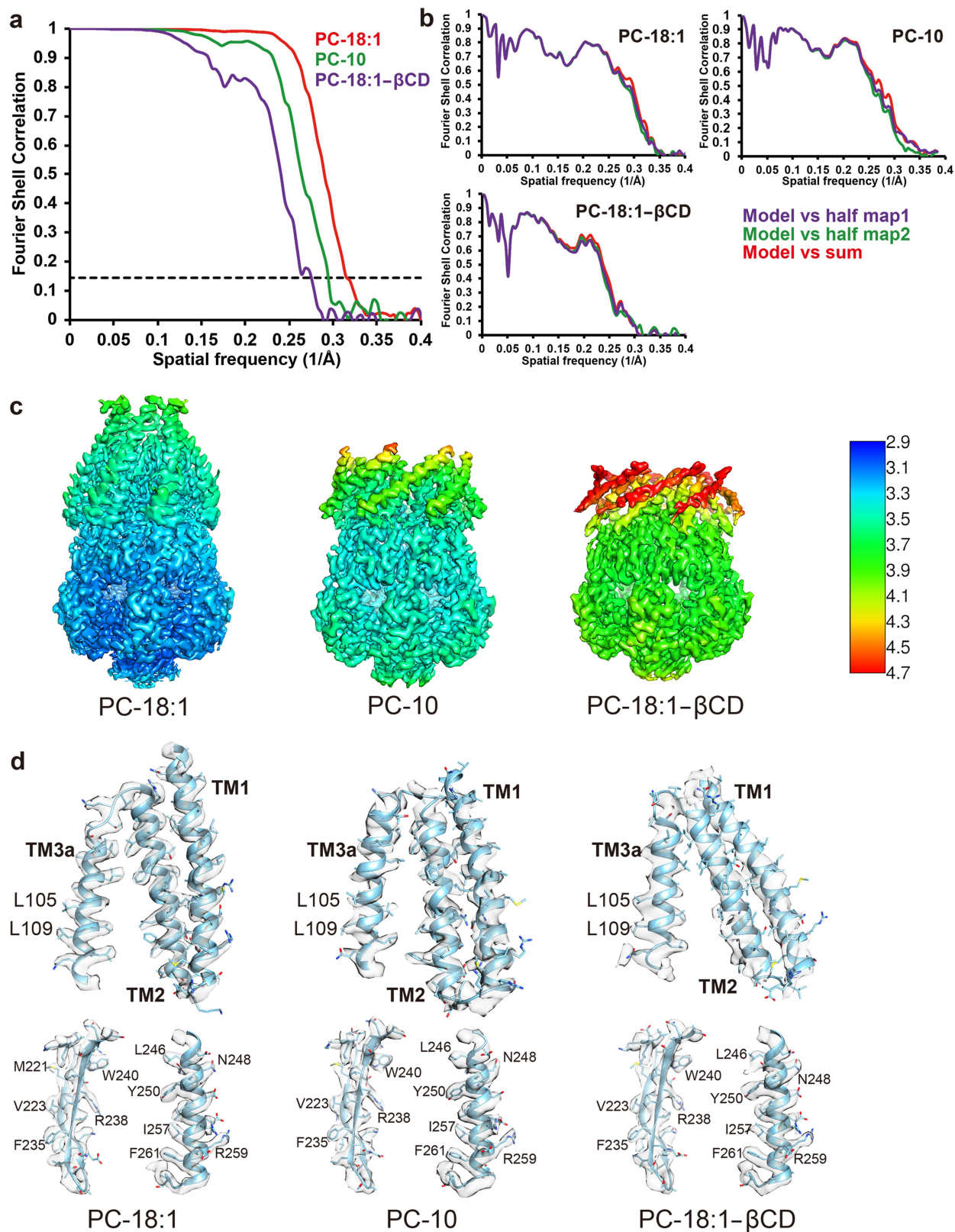
**Extended Data Fig. 3 | Image processing of MscS in PC-10 nanodiscs. a,** Area of an image of a vitrified sample. Some particles are circled. Scale bar, 50 nm. **b,** Selected 2D-class averages obtained with RELION-3. Side length of individual

averages, 20.8 nm. **c,** Image-processing workflow for 3D classification and refinement in RELION-3 that resulted in a density map at 3.4 Å resolution. See Methods and Extended Data Table 1 for details.



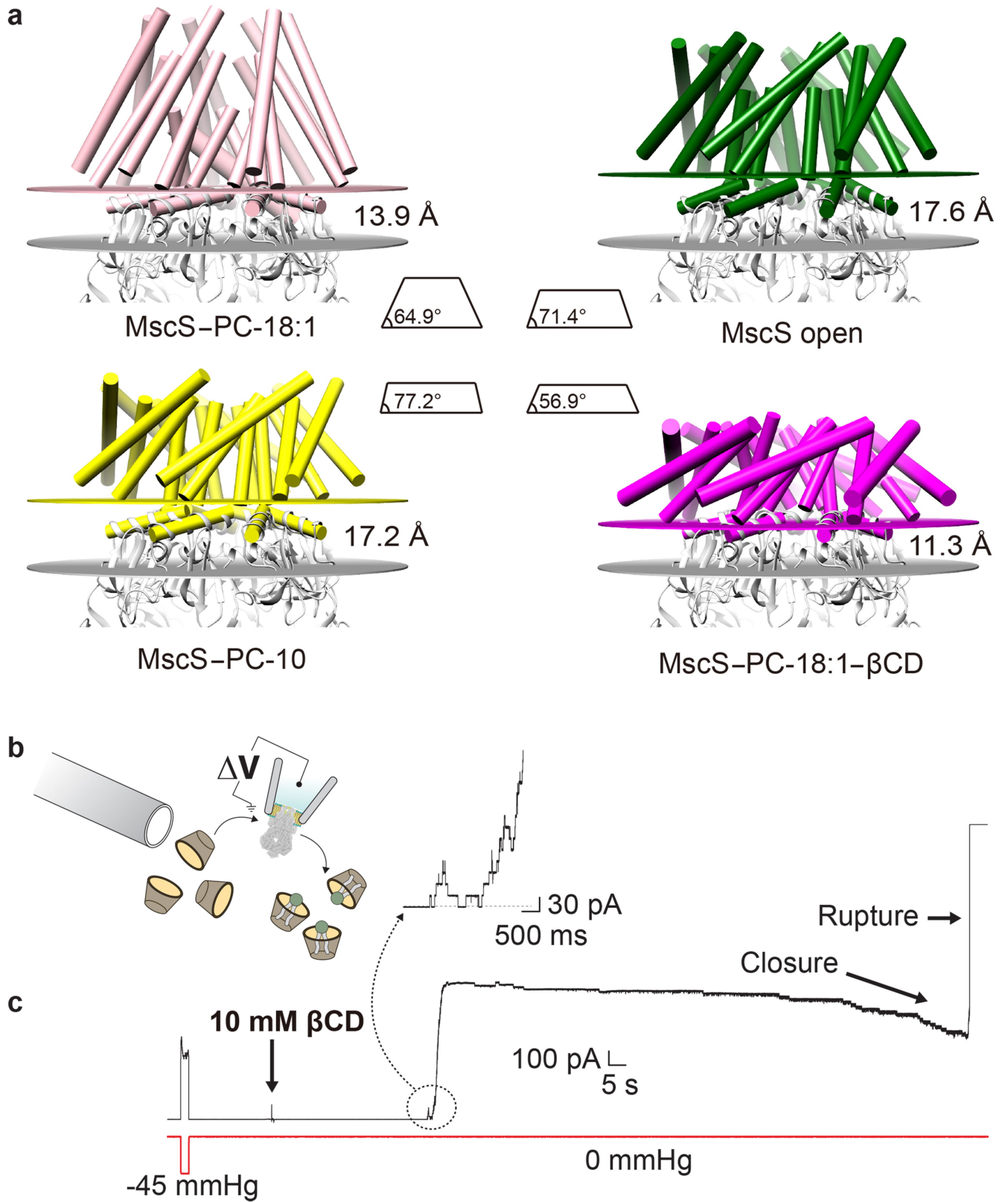
**Extended Data Fig. 4 | Treatment of nanodiscs with  $\beta$ CD and image processing of MscS in PC-18:1 nanodiscs after incubation with  $\beta$ CD for 16 h.** **a**, Negative-stain EM images of empty nanodiscs incubated with  $\beta$ CD at the conditions denoted, indicating that  $\beta$ CD can extract lipids from nanodiscs. Scale bar, 100 nm. Five to ten images were collected for each condition. **b**, Size-exclusion chromatogram of an MscS-PC-18:1 sample after incubation with 100 mM  $\beta$ CD for 16 h. The insets show negative-stain EM images of the two

peak fractions. Scale bar, 50 nm. Five images were collected for each peak fraction. **c**, Area of an image of a vitrified sample. Some particles are circled. Scale bar, 50 nm. **d**, Selected 2D-class averages obtained with RELION-3. Side length of individual averages, 21.6 nm. **e**, Image-processing workflow for 3D classification and refinement in RELION-3 that resulted in a density map at 3.7 Å resolution. See Methods and Extended Data Table 1 for details.



**Extended Data Fig. 5 | FSC curves, local-resolution maps and local densities.** **a**, FSC curves calculated between independently refined half maps for the MscS-PC-18:1 map (red), the MscS-PC-10 map (green), and the MscS-PC-18:1-βCD map (purple). **b**, Cross-validation FSC curves: purple, refined model versus half map 1 used for refinement (work map); green, refined model

versus half map 2 not used for refinement (free map); red, refined model versus the combined final map. The similarity of the 'work' and 'free' curves suggests no substantial over-fitting. **c**, Local-resolution maps for MscS-PC-18:1, MscS-PC-10, and MscS-PC-18:1-βCD. **d**, Local cryo-EM densities for MscS-PC-18:1, MscS-PC-10, and MscS-PC-18:1-βCD.

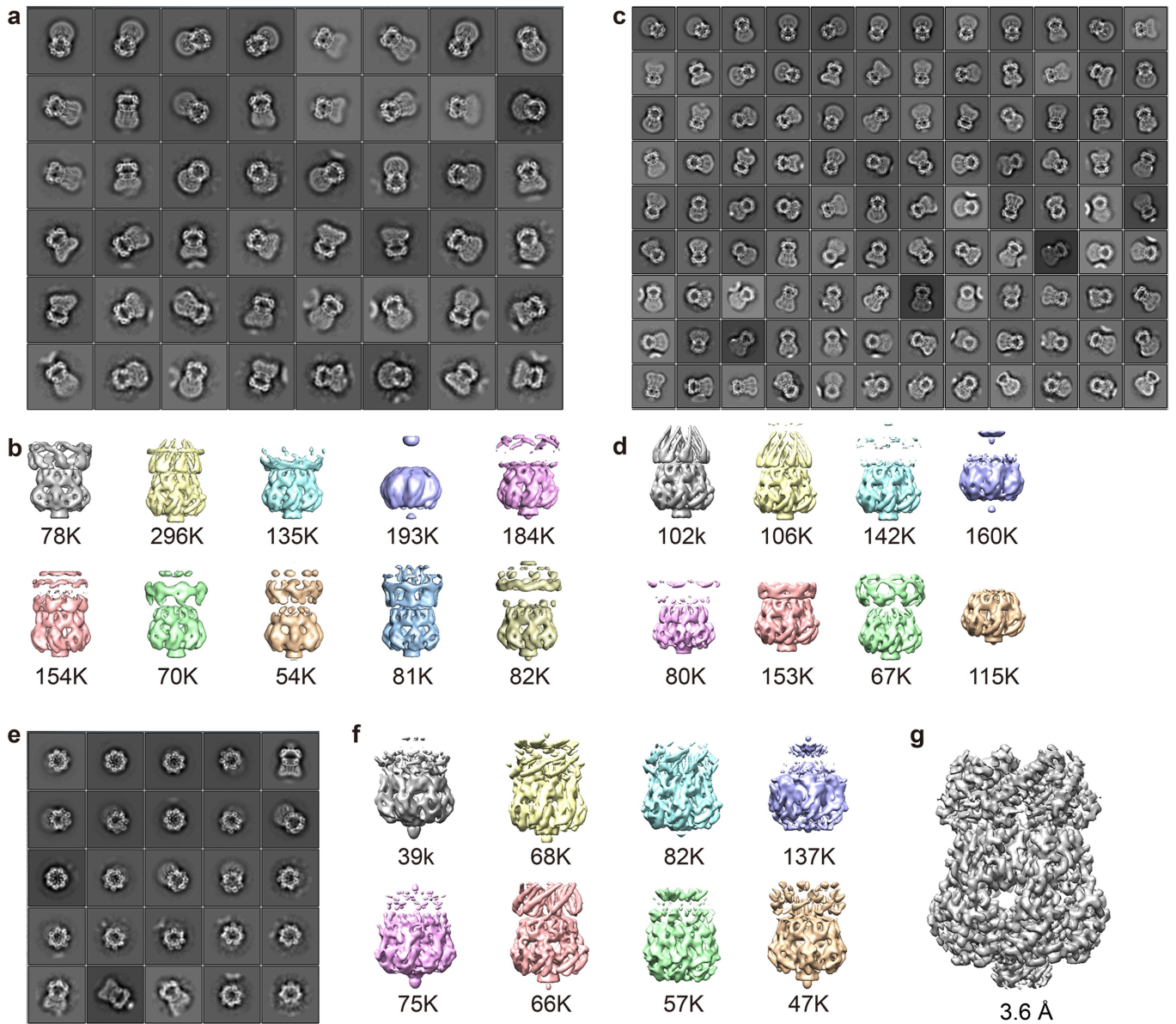


Extended Data Fig. 6 | See next page for caption.

# Article

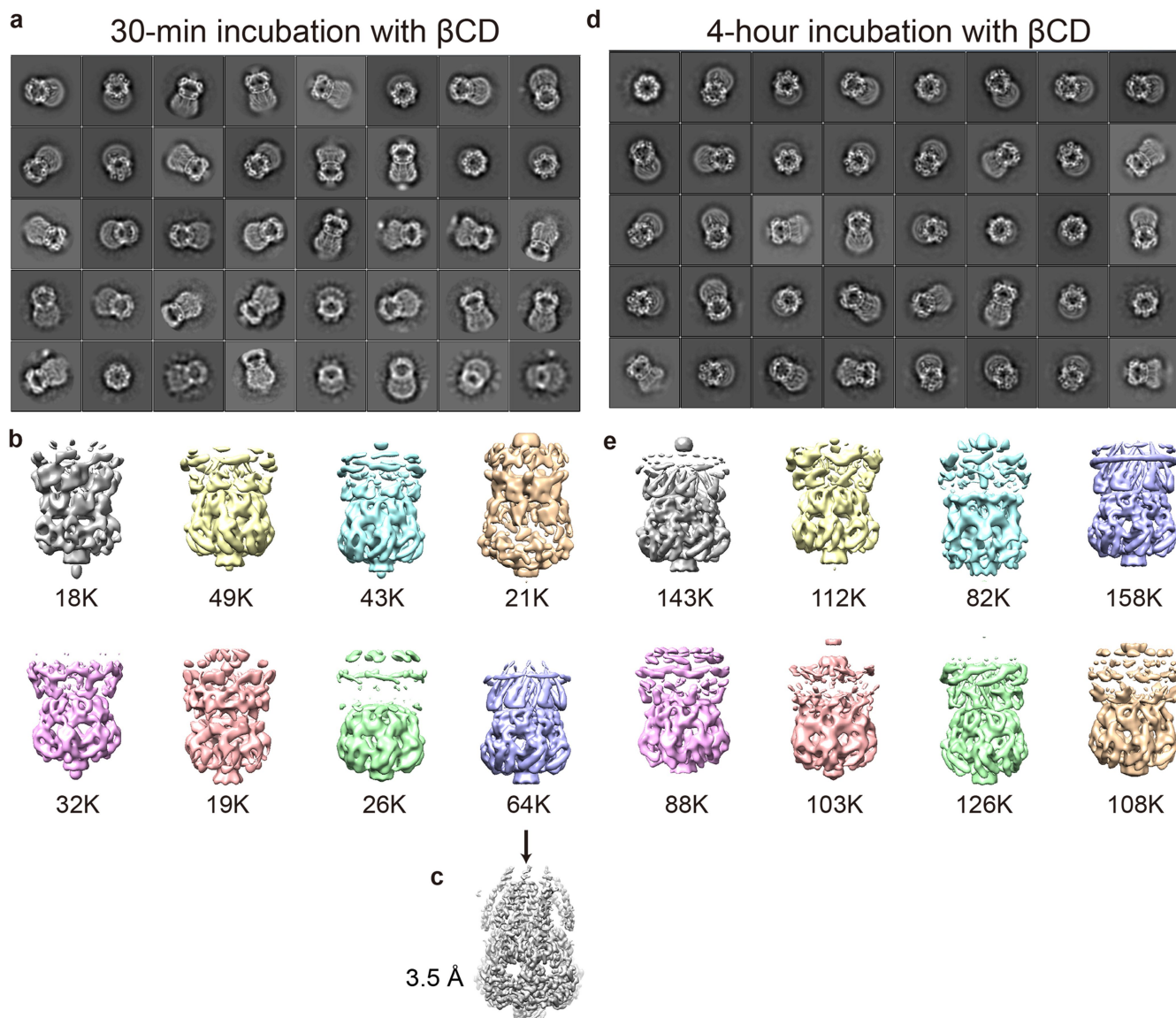
**Extended Data Fig. 6 | Distance between the cytoplasmic domain and TM1-TM2 in different MscS structures and  $\beta$ CD perfusion activates reconstituted MscS.** **a**, The numbers denote the distances between the plane of Leu146 (grey) in the middle  $\beta$  domain and the plane of Asp62 (coloured) at the start of TM2. TM1-TM2 and TM3a are shown as coloured cylinders, and TM3b and the middle  $\beta$  domain as grey ribbons. The trapezoids represent the overall shape of the TMD in the different conformations. The trapezoid shape is defined by the plane connecting Ser58 and Ala28 on TM1. Trapezoids with larger angles would fit better in flatter membranes. **b**, Set up of excised azolectin proteoliposomes and perfusion of  $\beta$ CD (brown). **c**, Exemplar trace

(black line) showing an initial application of a square wave negative pressure pulse of  $-45$  mmHg (red line) with a high-speed pressure clamp that activates a population of MscS channels at  $+30$  mV pipette potential, followed by the perfusion of  $10$  mM  $\beta$ CD and the subsequent activation of MscS with no further applied hydrostatic pressure.  $\beta$ CD alone without applied pressure activates the whole cohort of MscS channels in the excised patch with a prolonged plateau indicative of current saturation. Activation is followed by transition of the channel population towards a closed state and the experiment ends with the rupture of the membrane patch.



**Extended Data Fig. 7 | Two-dimensional class averages and 3D maps of MscS mutant proteins.** **a**, Two-dimensional class averages of the Gly113Ala MscS mutant in PC-18:1 nanodiscs after incubation with  $\beta$ CD for 16 h obtained with RELION-3. Side length of individual averages, 23.4 nm. While some classes show an extended and defined TMD as seen in 2D averages of MscS in the closed conformation or a compressed and smeared-out TMD or a compressed and asymmetric TMD, none of the classes shows a defined TMD architecture as the one seen in MscS-PC-18:1- $\beta$ CD. **b**, Three-dimensional maps of the Gly113Ala MscS mutant in PC-18:1 nanodiscs after incubation with  $\beta$ CD for 16 h obtained from 3D classification in RELION-3. None of the maps shows a TMD architecture similar to the one seen in MscS-PC-18:1- $\beta$ CD. **c**, Two-dimensional class averages of the Ala106Val MscS mutant in PC-18:1 nanodiscs obtained with RELION-3. Side length of individual averages, 21.6 nm. While some classes show an extended and defined TMD as seen in 2D averages of MscS in the closed

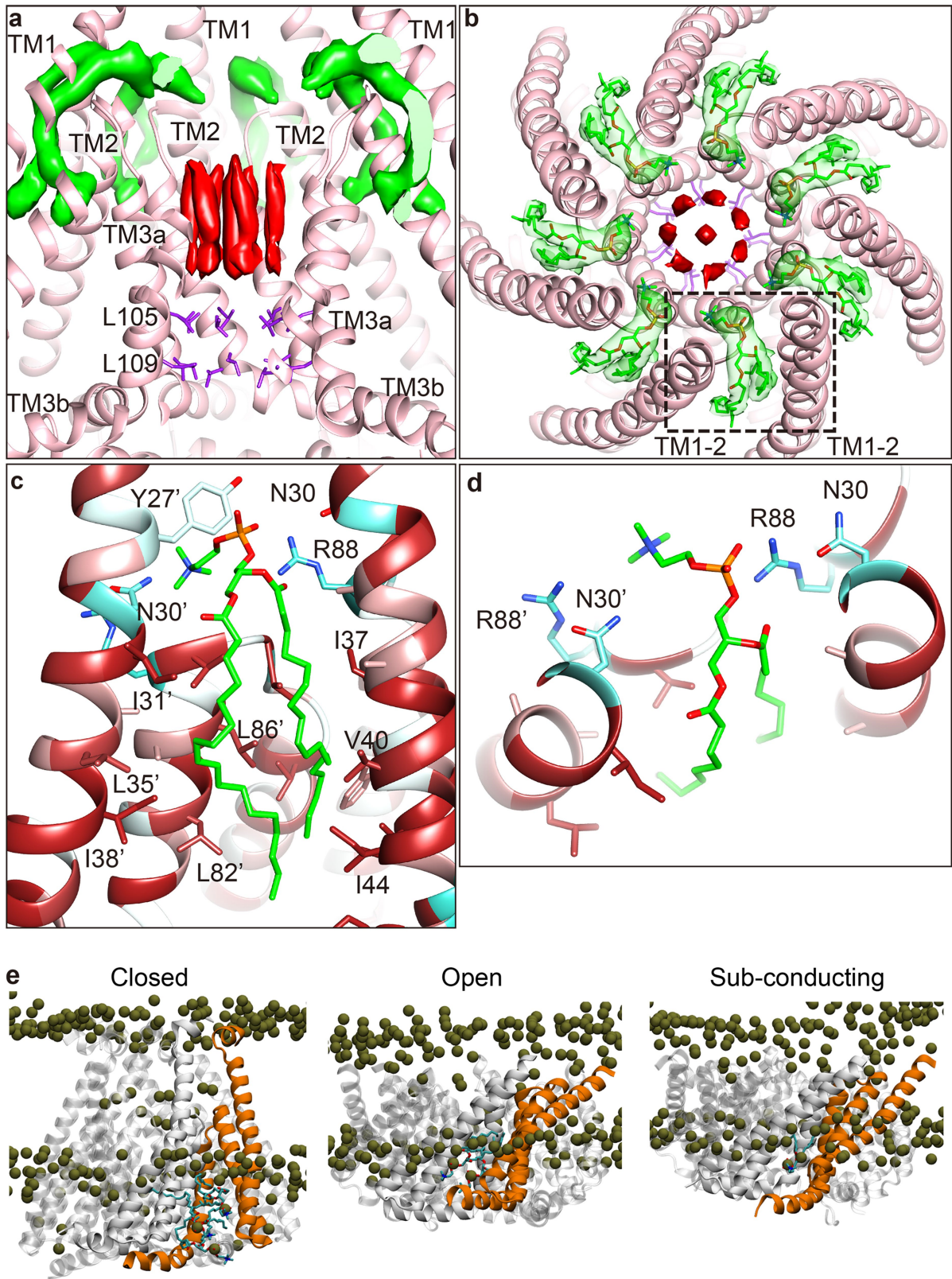
conformation, the TMD in classes with a compressed TMD is smeared out and/or asymmetric. **d**, Three-dimensional maps of the Ala106Val MscS mutant in PC-18:1 nanodiscs obtained from 3D classification in RELION-3. The only two maps with a defined TMD show MscS in the closed conformation (grey and yellow maps). None of the other maps has a well-defined TMD. Therefore, none of the maps shows MscS in the open conformation seen in the crystal structure of the Ala106Val mutant. **e**, Two-dimensional class averages of the Ala106Val MscS mutant in DDM obtained with RELION-3. Side length of individual averages, 20.8 nm. **f**, Three-dimensional maps of the Ala106Val MscS mutant in DDM obtained from 3D classification in RELION-3. The map with the best defined TMD (red) shows MscS in the same open conformation seen in the crystal structure of the Ala106Val mutant. **g**, Final map at 3.6 Å resolution after refining the map with the best defined TMD (red map in **b**).



**Extended Data Fig. 8 | Two-dimensional class averages and 3D maps of MscS in PC-18:1 nanodiscs after incubation with  $\beta$ CD for 30 min and 4 h.**

**a**, Two-dimensional class averages obtained with RELION-3 for MscS in PC-18:1 nanodiscs after a 30-min incubation with  $\beta$ CD. Side length of individual averages, 21.6 nm. Most classes show an extended and defined TMD as seen for MscS in the closed conformation. **b**, Three-dimensional maps for the MscS in PC-18:1 nanodiscs incubated for 30 min with  $\beta$ CD obtained from 3D classification in RELION-3. The map with the best defined TMD (purple) shows MscS in the closed conformation but with weaker density for TM1. None of the maps shows MscS in the open conformation seen in the crystal structure of the Ala106Val mutant. **c**, Final map at 3.5 Å resolution after refining the map with

the best defined TMD (purple map in **b**). **d**, Two-dimensional class averages obtained with RELION-3 for MscS in PC-18:1 nanodiscs after a 4-h incubation with  $\beta$ CD. Side length of individual averages, 21.6 nm. The class averages show different thicknesses for the TMD. **e**, Three-dimensional maps for the MscS in PC-18:1 nanodiscs incubated for 4 h with  $\beta$ CD obtained from 3D classification in RELION-3. The map with the best defined TMD (purple) shows MscS in the closed conformation but with weaker density for TM1. Another map with a well-defined TMD (grey) shows MscS in the closed conformation with slightly tilted TM1-TM2. None of the maps shows MscS in the open conformation seen in the crystal structure of the Ala106Val mutant.



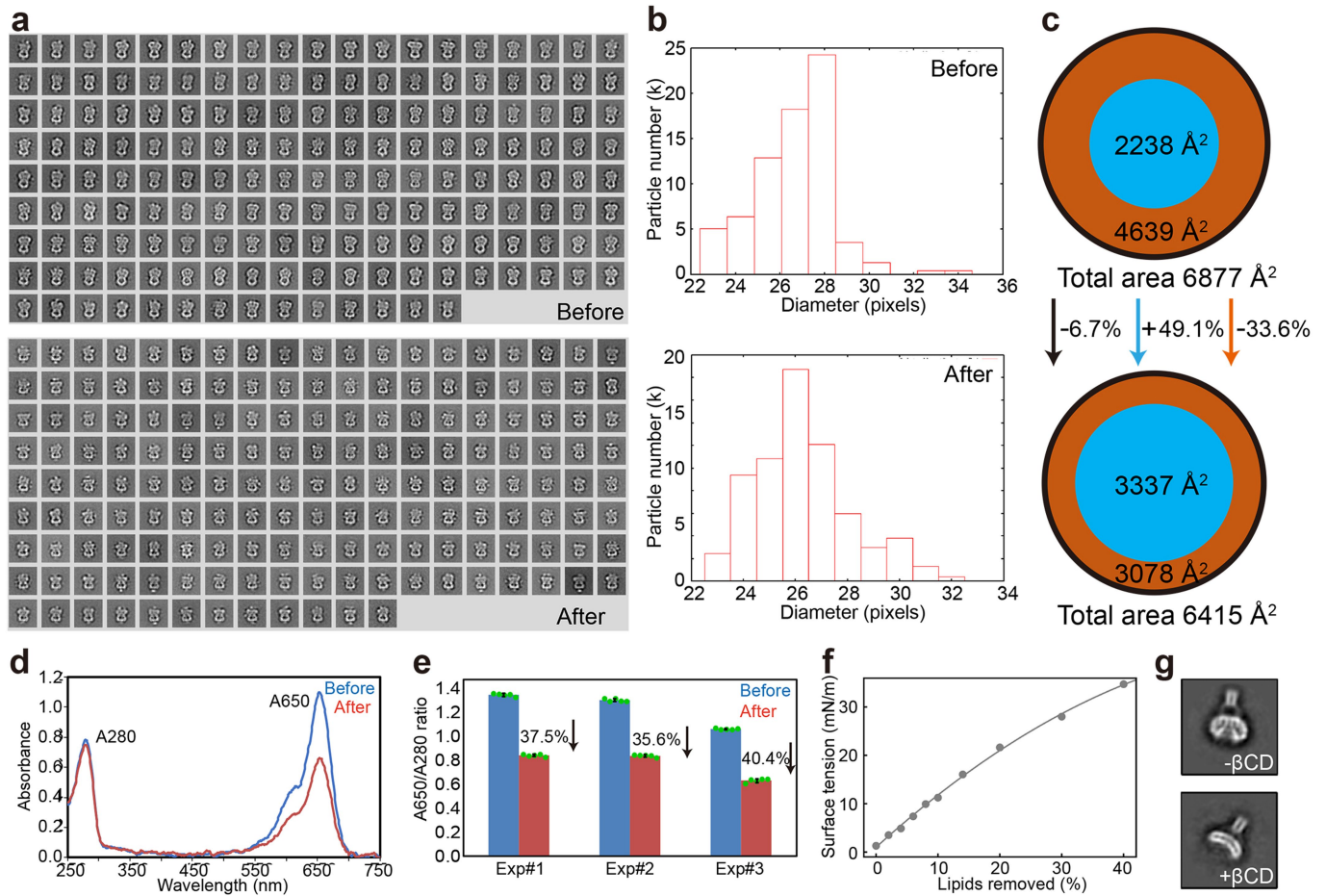
Extended Data Fig. 9 | See next page for caption.

# Article

## Extended Data Fig. 9 | Lipid densities in the map of MscS in PC-18:1

**nanodiscs and snapshots of MD simulations. a,** Cut-away side view of MscS-PC-18:1 colour-coded as in Fig. 4a. The side chains of gating residues Leu105 and Leu109 are shown as purple sticks. Densities for the pore lipids and the inverted gatekeeper lipids are shown in red and light green, respectively. **b,** Top view of MscS-PC-18:1 showing that the headgroups of the gatekeeper lipids (shown as green sticks in transparent green surface) are shielded from the membrane. **c, d,** Side view (**c**) and top view (**d**) of the area indicated by the dashed box in **b**, showing the residues interacting with the acyl chains (**c**) and headgroup (**d**) of

the gatekeeper lipid. The protein residues are coloured by hydrophobicity as in Extended Data Fig. 2c. **e,** The protein is shown as transparent white ribbon with two subunits forming a hydrophobic pocket shown in solid white and orange. For lipids other than those in the pockets, only the phosphorous atoms are shown as olive-green spheres. The lipids occupying the pocket formed by the orange subunits are shown in cyan stick representation with the phosphorous atoms as olive-green spheres. On average, each pocket holds  $3.3 \pm 0.2$  PC-18:1 lipids in the closed conformation,  $1.5 \pm 0.1$  PC-10 lipids in the open state, and  $0.6 \pm 0.1$  PC-10 lipid in the subconducting state.



### Extended Data Fig. 10 | Estimating the membrane tension in

**MscS-containing nanodiscs induced by  $\beta$ CD treatment.** **a**, The 2D-class averages of MscS in PC-18:1 nanodiscs before (upper panel) and after (lower panel) incubation with  $\beta$ CD obtained with the iterative stable alignment and clustering algorithm. Side length of individual averages, 22 nm. **b**, Distribution of nanodisc diameters measured from the averages shown in **a**. The average diameter of the MscS-containing nanodiscs is  $93.6 \pm 5.9$  Å before incubation with  $\beta$ CD and  $90.4 \pm 6.2$  Å after incubation with  $\beta$ CD. **c**, Surface areas occupied by MscS and PC-18:1 lipids in nanodiscs before (top) and after (bottom) incubation with  $\beta$ CD. On the basis of the measured diameters of MscS-containing nanodiscs before and after incubation with  $\beta$ CD, their surface areas (black circles) are  $6,877$  Å<sup>2</sup> [ $(46.8$  Å)<sup>2</sup>  $\times$   $3.14$ ] and  $6,415$  Å<sup>2</sup> [ $(45.2$  Å)<sup>2</sup>  $\times$   $3.14$ ], respectively. The areas occupied by the TMD of MscS (blue areas) in the closed and desensitized states (estimated on the basis of the position of Leu35 in the middle of the transmembrane region of TMI) are very different, namely  $2,238$  Å<sup>2</sup> [ $(26.7$  Å)<sup>2</sup>  $\times$   $3.14$ ] for MscS in the closed conformation and  $3,337$  Å<sup>2</sup> [ $(32.6$  Å)<sup>2</sup>  $\times$   $3.14$ ] for MscS in the desensitized conformation. Therefore, the areas occupied by lipids (brown areas) in nanodiscs containing MscS in the

closed conformation are  $4,639$  Å<sup>2</sup> [ $6,877$  Å<sup>2</sup>  $-$   $2,238$  Å<sup>2</sup>] and  $3,078$  Å<sup>2</sup> [ $6,415$  Å<sup>2</sup>  $-$   $3,337$  Å<sup>2</sup>] in nanodiscs containing MscS in the desensitized conformation. In summary, incubation with  $\beta$ CD reduces the total area of the nanodiscs (black circles) by only 6.7%, but because the area occupied by MscS increases by 49.1%, the area occupied by the lipids shrinks by 33.6%. **d**, Representative NanoDrop spectra recorded for MscS-containing nanodiscs with Cy5-labelled PC-18:1 before (blue trace) and after (red trace) incubation with  $\beta$ CD. The ratio of absorbance at 280 nm (MscS) and at 650 nm (Cy5-labelled PC-18:1) was measured to estimate lipid removal. **e**, Changes in the Cy5-lipid:protein ratio upon incubation of MscS-containing nanodiscs with  $\beta$ CD in three independent experiments. The five individual measurements are shown as green dots. The columns show the averages and the error bars represent the standard deviations. **f**, Graph of the membrane tension as a function of the percentage of removed lipids determined by MD simulations. Trajectories were divided into blocks of 0.1  $\mu$ s to evaluate the average and the standard error of the mean (s.e.m.). The s.e.m. in the plot is smaller than the size of the dots. **g**, Selected 2D-class averages of MscS-containing nanodiscs before (top) and after (bottom)  $\beta$ CD treatment. Side length of individual averages, 20.8 nm.

# Article

**Extended Data Table 1 | Cryo-EM data collection, refinement and validation statistics**

	MscS-PC-18:1 (EMDB-21462) (PDB 6VYK)	MscS-PC-10 (EMDB-21463) (PDB 6VYL)	MscS-PC-18:1- $\beta$ CD (EMDB-21464) (PDB 6VYM)	MscS-PC-18:1- $\beta$ CD(30min) (EMDB-21465)	MscS(Ala106Val)- DDM (EMDB-21466)
<b>Data collection and processing</b>					
Microscope	Titan Krios	Titan Krios	Titan Krios	Titan Krios	Titan Krios
Voltage (kV)	300	300	300	300	300
Camera	K2	K2	K2	K2	K2
Magnification	28,000	22,500	28,000	28,000	22,500
Pixel size (Å)	1.0	1.3	1.0	1.0	1.3
Dose rate (e <sup>-</sup> /s/pixel)	6	8	6	6	8
Exposure time (s)	10	10	10	10	10
Frame rate (ms)	250	250	250	250	250
Electron exposure (e <sup>-</sup> /Å <sup>2</sup> )	55	47	55	55	47
Defocus range (μm)	-1.2~-2.5	-1.2~-2.5	-1.2~-2.5	-1.2~-2.5	-1.2~-2.5
Movie stacks (no.)	1870	3794	2178	1384	1571
Boxsize (pixels)	216	160	216	216	160
Initial particle images (no.)	630,667	1,833,905	1,119,795	619,665	1,263,398
Final particle images (no.)	98,111	86,609	51,333	64,153	66,051
Symmetry imposed	C7	C7	C7	C7	C7
Map resolution (Å)	3.17	3.4	3.66	3.5	3.6
FSC threshold	0.143	0.143	0.143	0.143	0.143
Map resolution range (Å)	2.9-4	3.1-4.1	3.5-5	3.2-4.5	3.2-4.1
<b>Refinement</b>					
Initial model used (PDB code)	2AOU	2VV5	2AOU		
Map sharpening <i>B</i> factor (Å <sup>2</sup> )	-170	-160	-209	-171	-173
<b>Model composition</b>					
Non-hydrogen atoms	14245	13685	13573		
Protein residues	1869	1799	1778		
Ligands	7				
<b><i>B</i> factors (Å<sup>2</sup>)</b>					
Protein	33.4	37.6	83.9		
Ligand	60.4				
<b>rms deviations</b>					
Bond lengths (Å)	0.008	0.009	0.007		
Bond angles (°)	1.19	1.18	1.17		
<b>Validation</b>					
MolProbity score	1.42	1.6	1.8		
Clashscore	3.12	4.71	6.26		
Poor rotamers (%)	0	0.48	0		
<b>Ramachandran plot</b>					
Favored (%)	95.47	94.88	92.66		
Allowed (%)	4.53	5.12	7.14		
Disallowed (%)	0	0	0		

## Reporting Summary

Nature Research wishes to improve the reproducibility of the work that we publish. This form provides structure for consistency and transparency in reporting. For further information on Nature Research policies, see [Authors & Referees](#) and the [Editorial Policy Checklist](#).

### Statistics

For all statistical analyses, confirm that the following items are present in the figure legend, table legend, main text, or Methods section.

n/a Confirmed

- |                                     |                                     |  |
|-------------------------------------|-------------------------------------|--|
| <input type="checkbox"/>            | <input checked="" type="checkbox"/> | The exact sample size ( $n$ ) for each experimental group/condition, given as a discrete number and unit of measurement  |
| <input type="checkbox"/>            | <input checked="" type="checkbox"/> | A statement on whether measurements were taken from distinct samples or whether the same sample was measured repeatedly  |
| <input type="checkbox"/>            | <input checked="" type="checkbox"/> | The statistical test(s) used AND whether they are one- or two-sided<br><i>Only common tests should be described solely by name; describe more complex techniques in the Methods section.</i>   |
| <input checked="" type="checkbox"/> | <input type="checkbox"/>            | A description of all covariates tested   |
| <input checked="" type="checkbox"/> | <input type="checkbox"/>            | A description of any assumptions or corrections, such as tests of normality and adjustment for multiple comparisons  |
| <input type="checkbox"/>            | <input checked="" type="checkbox"/> | A full description of the statistical parameters including central tendency (e.g. means) or other basic estimates (e.g. regression coefficient) AND variation (e.g. standard deviation) or associated estimates of uncertainty (e.g. confidence intervals) |
| <input checked="" type="checkbox"/> | <input type="checkbox"/>            | For null hypothesis testing, the test statistic (e.g. $F$ , $t$ , $r$ ) with confidence intervals, effect sizes, degrees of freedom and $P$ value noted<br><i>Give <math>P</math> values as exact values whenever suitable.</i>                            |
| <input checked="" type="checkbox"/> | <input type="checkbox"/>            | For Bayesian analysis, information on the choice of priors and Markov chain Monte Carlo settings   |
| <input checked="" type="checkbox"/> | <input type="checkbox"/>            | For hierarchical and complex designs, identification of the appropriate level for tests and full reporting of outcomes   |
| <input checked="" type="checkbox"/> | <input type="checkbox"/>            | Estimates of effect sizes (e.g. Cohen's $d$ , Pearson's $r$ ), indicating how they were calculated   |

*Our web collection on [statistics for biologists](#) contains articles on many of the points above.*

### Software and code

Policy information about [availability of computer code](#)

Data collection	SerialEM, pCLAMP 10
Data analysis	Relion 3.0, Gautomatch 0.56, Ctffind 1.08, Chimera 1.12, ChimeraX 0.9, I-Tasser, Coot 0.8.9, Phenix 1.17.1, GROMACS2019, CHARMM36m, HOLE

For manuscripts utilizing custom algorithms or software that are central to the research but not yet described in published literature, software must be made available to editors/reviewers. We strongly encourage code deposition in a community repository (e.g. GitHub). See the Nature Research [guidelines for submitting code & software](#) for further information.

### Data

Policy information about [availability of data](#)

All manuscripts must include a [data availability statement](#). This statement should provide the following information, where applicable:

- Accession codes, unique identifiers, or web links for publicly available datasets
- A list of figures that have associated raw data
- A description of any restrictions on data availability

The cryo-EM maps have been deposited in the Electron Microscopy Data Bank under accession codes EMD-21462 (MscS-PC-18:1), EMD-21463 (MscS-PC-10), EMD-21464 (MscS-PC-18:1-βCD), EMD-21465 (MscS-PC-18:1-βCD-30min), and EMD-21466 (MscS(Ala106Val)-DDM). Atomic coordinates have been deposited in the Protein Data Bank under accession codes 6VYK (MscS-PC-18:1), 6VYL (MscS-PC-10), and 6VYM (MscS-PC-18:1-βCD).

## Field-specific reporting

Please select the one below that is the best fit for your research. If you are not sure, read the appropriate sections before making your selection.

Life sciences     Behavioural & social sciences     Ecological, evolutionary & environmental sciences

For a reference copy of the document with all sections, see [nature.com/documents/nr-reporting-summary-flat.pdf](https://www.nature.com/documents/nr-reporting-summary-flat.pdf)

## Life sciences study design

All studies must disclose on these points even when the disclosure is negative.

Sample size	Sample sizes for the Cryo-EM datasets were determined by the need to obtain meaningful structures and the availability of cryo-EM time. For the MscS-PC-18:1 dataset, 1870 movie stacks were collected and 98,111 particles were used for the final reconstruction, which was sufficient to yield a 3.17-Å resolution structure. For the MscS-PC-10 dataset, 3794 movie stacks were collected and 86,609 particles were used for the final reconstruction, which was sufficient to yield a 3.4-Å resolution structure. For the MscS-PC-18:1-βCD dataset, 2178 movie stacks were collected and 51,333 particles were used for the final reconstruction, which was sufficient to yield a 3.66-Å resolution structure.
Data exclusions	Micrographs clearly suffering from astigmatism, image drift, ice contamination and/or cubic ice formation were excluded from the datasets. Particles in 2D classes showing no secondary structural features and in 3D classes showing unsatisfactory structural features were excluded from the final reconstructions.
Replication	For the high-resolution structures obtained in this study, small datasets were first collected on a 200-kV Talos Arctica electron microscope. The structures were then confirmed and improved by data collection on a 300-kV Titan Krios electron microscope.
Randomization	In the 3D refinement, particle images were randomly split into two half groups.
Blinding	Blinding is not applicable to structure determination by single-particle cryo-EM.

## Reporting for specific materials, systems and methods

We require information from authors about some types of materials, experimental systems and methods used in many studies. Here, indicate whether each material, system or method listed is relevant to your study. If you are not sure if a list item applies to your research, read the appropriate section before selecting a response.

### Materials & experimental systems

n/a	Involvement in the study
<input checked="" type="checkbox"/>	<input type="checkbox"/> Antibodies
<input checked="" type="checkbox"/>	<input type="checkbox"/> Eukaryotic cell lines
<input checked="" type="checkbox"/>	<input type="checkbox"/> Palaeontology
<input checked="" type="checkbox"/>	<input type="checkbox"/> Animals and other organisms
<input checked="" type="checkbox"/>	<input type="checkbox"/> Human research participants
<input checked="" type="checkbox"/>	<input type="checkbox"/> Clinical data

### Methods

n/a	Involvement in the study
<input checked="" type="checkbox"/>	<input type="checkbox"/> ChIP-seq
<input checked="" type="checkbox"/>	<input type="checkbox"/> Flow cytometry
<input checked="" type="checkbox"/>	<input type="checkbox"/> MRI-based neuroimaging